

4-2019

## Metamaterial-Based Sensor Design Using Split Ring Resonator and Hilbert Fractal for Biomedical Application

Nadin M. N. Alrayes

Follow this and additional works at: [https://scholarworks.uaeu.ac.ae/electric\\_theses](https://scholarworks.uaeu.ac.ae/electric_theses)



Part of the [Engineering Commons](#)

---

### Recommended Citation

N. Alrayes, Nadin M., "Metamaterial-Based Sensor Design Using Split Ring Resonator and Hilbert Fractal for Biomedical Application" (2019). *Electrical Engineering Theses*. 10.  
[https://scholarworks.uaeu.ac.ae/electric\\_theses/10](https://scholarworks.uaeu.ac.ae/electric_theses/10)

This Thesis is brought to you for free and open access by the Electrical Engineering at Scholarworks@UAEU. It has been accepted for inclusion in Electrical Engineering Theses by an authorized administrator of Scholarworks@UAEU. For more information, please contact [fadl.musa@uaeu.ac.ae](mailto:fadl.musa@uaeu.ac.ae).



United Arab Emirates University

College of Engineering

Department of Electrical Engineering

METAMATERIAL-BASED SENSOR DESIGN USING SPLIT RING  
RESONATOR AND HILBERT FRACTAL FOR BIOMEDICAL  
APPLICATION

Nadin M. N. Alrayes

This thesis is submitted in partial fulfillment of the requirements for the degree of  
Master of Science in Electrical Engineering

Under the Supervision of Prof. Mousa Hussein

April 2019

## Declaration of Original Work

I, Nadin M. N. Alrayes, the undersigned, a graduate student of United Arab Emirates University (UAEU), and the author of this thesis entitled “*Metamaterial-Based Sensor Design Using Split Ring Resonator and Hilbert Fractal for Biomedical Application*,” hereby solemnly declare that this thesis is my own original research that has been conducted and prepared under the supervision of Prof. Mousa Hussein in the College of Engineering at UAEU. This work has not been presented or published previously or has not formed the basis for the award of any academic degree, diploma, or similar title at this or any other university. Any materials borrowed from other sources (whether published or unpublished) and relied upon or included in my thesis have been properly cited and acknowledged in accordance with appropriate academic conventions. I further declare no potential conflict of interest with respect to the research, data collection, authorship, presentation, and/or publication of this thesis.

Student's Signature: \_\_\_\_\_ 

Date: 2015/2019

### Approval of the Master Thesis

This Master Thesis is approved by the following Examining Committee Members:

1) Advisor (Committee Chair): Prof. Mousa Hussein

Title: Associate Professor

Department of Electrical Engineering

College of Engineering

Signature 

Date 21/4/2019

2) Member: Prof. Saleh Thaker

Title: Professor

Department of Physics

College of Science

Signature 

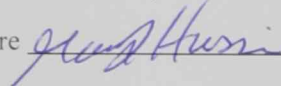
Date 21/4/2019

3) Member (External Examiner): Prof. Derek Abbott

Title: Professor

Department: School of Electrical & Electronic Engineering

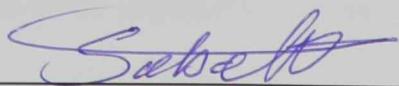
Institution: University of Adelaide, Australia

Signature 

Date 21/4/2019

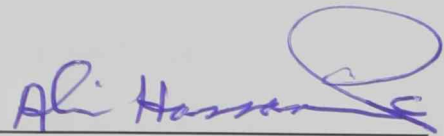
This Master Thesis is accepted by:

Dean of the College of Engineering: Prof. Sabah Alkass

Signature 

Date 20/5/2019

Acting Dean of the College of Graduate Studies: Prof. Ali Al-Marzouqi

Signature 

Date 21/5/2019

Copy 8 of 8

Copyright © 2019 Nadin M. N. Alrayes  
All Rights Reserved

## Abstract

In this research, a simple and efficient approach is presented to design a metamaterial-based sensitive sensor for biomedical applications. The metamaterial-based sensor is designed to differentiate between different types of cancer cell lines based on their electrical properties. The sensor is designed by incorporating a single circular split ring resonator (SRR) and a Hilbert fractal curve. The SRR is used considering its capacitive and inductive resonance properties, thereby making the SRR a favorable candidate for sensing applications. Moreover, the Hilbert fractal curve was used as a defected ground structure to increase sensor sensitivity and selectivity. The Hilbert fractal ground will increase the capacitance and inductance of the sensor, thus increasing the sensor sensitivity. Different Hilbert curve orders were investigated. The fourth-order Hilbert curve was used in the final design because it showed the optimal performance among the orders. To verify the sensor functionality and selectivity, the proposed sensor was tested through three breast cancer cell lines. Measurement results were compared to simulated results obtained using high-frequency structure simulator (HFSS). In addition, support vector machine, which is an artificial neural network (ANN), was developed to classify the type of each cancerous cell based on resonance frequency.

**Keywords:** Metamaterial, split ring resonator, Hilbert defected ground structure, biosensor.

## Title and Abstract (in Arabic)

تصميم مستشعر مرتكز على مواد استثنائية الخصائص باستخدام رنان حلقي و منحني

هيلبرت للتطبيقات الطبية الحيوية

### الملخص

خلال هذا البحث تم تصميم مستشعر لأغراض الطبية حيث أن بإمكان المستشعر التمييز بين أنواع مختلفة من الخلايا السرطانية بناءً على خواصهم الكهربائية. التصميم الأساسي للمستشعر قائم على استخدام نوع من أنواع المواد استثنائية الخصائص (Metamaterial) و هي الحلقة الدائرية الرنانة ذات الشق بالإضافة إلى استخدام منحني هيلبرت الكسري. استخدمت الحلقة الرنانة لخواصها كمستحث و مكثف حيث أنها تنتج تردد الرنين. القيم الناتجة للتردد هي ما تم استخدامه للتمييز ما بين أنواع الخلايا المختبرة. استخدم منحني هيلبرت الكسري في تصميم لوح التآريض حيث أن حفر المنحني أدى لزيادة قيمة المستحث و المكثف للمستشعر و بالتالي أدى لزيادة حساسية المستشعر و انتقائيته. خلال البحث تمت دراسة درجات مختلفة من منحني هيلبرت و من خلال النتائج وُجدَ أن أفضل أداء كان أداء الدرجة الرابعة للمنحني الكسري. لاختبار فعالية المستشعر و إنتقائيته تمت تجربة ثلاثة أنواع من الخلايا السرطانية و مقارنة النتائج المختبرية مع نتائج برنامج المحاكاة HFSS. تم تطوير شعاع الدعم الآلي و هي عبارة عن شبكة أعصاب اصطناعية استخدمت لتصنيف أنواع الخلايا السرطانية بناءً على ترددهم الرنيني.

**مفاهيم البحث الرئيسية:** المواد استثنائية الخصائص, الحلقة الرنانة ذات الشق, منحني هيلبرت الكسري, المستشعر الطبي.



## **Acknowledgments**

I would like to thank my thesis advisor Dr. Mousa Hussein for his patience and guidance. He was always available for help when I needed it and steered me in the right direction throughout the research. With his immense knowledge and valuable comments, this research would not have been possible. I would like to acknowledge Dr. Rabah Iratni and his team for their collaboration in preparing the cell lines, and Eng. Abdulrahman Daher for his time and help in fabricating the sensor.

I must acknowledge with profound gratitude the motivation and support of my beloved parents and siblings for encouraging me throughout my years of study. This accomplishment would not have been possible without them. Thank you.

## Dedication

*To my family and friends*

*Thank you, I could not have done this endeavor without you.*

## Table of Contents

Title .....	i
Declaration of Original Work .....	ii
Copyright .....	iii
Approval of the Master Thesis .....	iv
Abstract .....	vi
Title and Abstract (in Arabic) .....	vii
Acknowledgments .....	viii
Dedication .....	ix
Table of Contents .....	x
List of Figures .....	xii
List of Tables.....	xv
List of Abbreviations.....	xvi
Chapter 1: Introduction .....	1
1.1 Statement of the Problem .....	1
1.2 Research Objectives .....	1
1.2.1 Sensor Characterization .....	2
1.3 Overview .....	2
1.3.1 Metamaterial .....	4
1.3.2 Fractal Hilbert Curve.....	5
1.3.3 Reflection and Transmission Coefficient.....	6
1.3.4 High-Frequency Structure Simulator (HFSS).....	7
1.3.5 Vector Network Analyzer (VNA).....	7
1.3.6 Electrical Properties of Cancer Cell Lines .....	7
1.3.7 Different Defected Ground Topographies .....	9
1.3.8 Support Vector Machine (SVM).....	10
Chapter 2: Literature Review .....	11
Chapter 3: Design Methods and Analysis.....	23
3.1 Theoretical Model and Design.....	23
3.1.1 SRR .....	23
3.1.2 Perturbed Hilbert Ground.....	25
3.1.3 Combined Design.....	26

3.2 Simulated Model .....	27
3.2.1 SRR .....	27
3.2.2 Perturbed Hilbert Curve .....	29
3.2.3 Combined Design .....	30
3.3 Simulated Response of the Sensor .....	32
Chapter 4: Results and Discussion .....	35
4.1 Sensor Fabrication .....	35
4.2 Cell Culture and Sample Preparation .....	36
4.3 Lab Measurement Instrument and Procedure .....	37
4.3.1 VNA Calibration .....	37
4.3.2 System Setup .....	38
4.3.3 Measurement Results .....	39
4.4 Cell Type Classification .....	44
Chapter 5: Conclusion and Future Work .....	49
References .....	51

## List of Figures

Figure 1: Open-ended waveguide for sensing application.....	3
Figure 2: Open-ended coaxial probe for sensing application.....	3
Figure 3: Split ring resonator designs .....	5
Figure 4: Hilbert curve .....	6
Figure 5: Real part of the complex dielectric constant with respect to frequency for different breast cell lines .....	8
Figure 6: Tangent loss with respect to frequency for different breast cell lines. ....	9
Figure 7: Magnetic field for different orders .....	10
Figure 8: Electrical field for different orders .....	10
Figure 9: Structure of the optical system module .....	11
Figure 10: Multi split ring resonator sensor.....	12
Figure 11: Double split ring resonator sensor .....	13
Figure 12: Classical structure.....	13
Figure 13: Nested structure .....	13
Figure 14: I-shaped structure .....	14
Figure 15: Crossed-I shaped structure.....	14
Figure 16: Multi-SRR sensor .....	14
Figure 17: Double SRR sensor.....	15
Figure 18: Transducer layout .....	16
Figure 19: Three transducer topographies.....	17
Figure 20: Tapped circular SRR .....	17
Figure 21: Sensor layout, the black areas are the etched out regions, and the white areas are the conductor .....	18
Figure 22: CSRR-loaded SIW cavity.....	19

Figure 23: Flexible Hilbert curve loop antenna .....	20
Figure 24: Hilbert curve used in designing a soil moisture sensor .....	21
Figure 25: Fabricated Hilbert antenna.....	22
Figure 26: Structures used in the design. ....	23
Figure 27: LC circuit.....	23
Figure 28: Perturbed Hilbert curve. ....	26
Figure 29: Equivalent circuit of the SRR and the DGS. ....	27
Figure 30: SRR unit cell.....	28
Figure 31: Simulated reflection coefficient of the SRR.....	28
Figure 32: SRR unit cell simulation.....	29
Figure 33: Simulated reflection coefficient of the DGS. ....	29
Figure 34: Sensor design.....	30
Figure 35: Simulated reflection coefficient of the final design.....	31
Figure 36: S <sub>21</sub> of the SRR with different aperture Hilbert curve orders.....	32
Figure 37: Sensor model with a sample of a cancer cell line.....	32
Figure 38: Simulated S <sub>12</sub> in magnitude.....	33
Figure 39: Simulated S <sub>12</sub> in degree angle. ....	34
Figure 40: Schematic of the measurement setup. ....	35
Figure 41: MITS Auto Lab. ....	36
Figure 42: Top and bottom views of the sensors .....	36
Figure 43: Lab measurement instruments .....	37
Figure 44: Measurement setup .....	39
Figure 45: Measured S <sub>12</sub> in magnitude .....	39
Figure 46: Measured S <sub>12</sub> in phase angles.....	40
Figure 47: Transmission coefficient of vacuum.....	41

Figure 48: Transmission coefficient of MDA-MB-231 .....	41
Figure 49: Transmission coefficient of MCF-7 .....	42
Figure 50: Transmission coefficient of HS578-T .....	42
Figure 51: One-versus-one multiclassification method .....	45
Figure 52: Classification Learner .....	46
Figure 53: Linear SVM scatterplot .....	46
Figure 54: Classified resonance frequencies .....	47
Figure 55: Averaged response of MCF-7 and its confidence interval .....	47
Figure 56: Averaged response of MDA-MB-231 and confidence interval.....	48
Figure 57: Averaged response of HS578-T and its confidence interval .....	48
Figure 58: Averaged response of vacuum and its confidence interval .....	48

## List of Tables

Table 1: Parameters used to design the SRR .....	25
Table 2: Parameters used to design the Hilbert curve.....	25
Table 3: Parameters used to design the perturbed Hilbert curve .....	26
Table 4: Shift in frequency with respect to the vacuum's resonance frequency.....	34
Table 5: Lab measurement .....	43
Table 6: Variation in the resonance frequency of the lab measured values with respect to different references.....	44
Table 7: Resonance frequencies used as a training set (GHz) .....	45



## List of Abbreviations

ANN	Artificial Neural Network
ATCC	American Type Culture Collection
CNC	Computer Numerical Control
CSRR	Complementary Split Ring Resonator
DGS	Defected Ground Structure
DNA	Deoxyribonucleic Acid
HFSS	High-Frequency Structure Simulator
miRNA	Micro-Ribonucleic Acid
MRI	Magnetic Resonance Imaging
PBS	Phosphate-Buffered Saline
PCB	Printed Circuit Board
SIW	Substrate-Integrated Waveguide
SMA	Sub Miniature Version A
SOLT	Short Open Load Through
S-parameters	Scattering parameters
SRR	Split Ring Resonator
SVM	Support Vector Machine
UHF	Ultra-High Frequency
UV	Ultraviolet
VNA	Vector Network Analyzer

## **Chapter 1: Introduction**

### **1.1 Statement of the Problem**

Early detection of cancer can make the treatment process effective. Mammography and ultrasound are popular modalities used to detect breast cancer. A mammogram is an imaging method that requires a low dose of x-ray to diagnose breast diseases, whereas ultrasound requires high-frequency sound waves. However, these methods have a false negative screening rate of 10% [1]. Such methods are selected on the basis of patients' situation; for example, pregnant women are prohibited from being exposed to x-rays [2]. Other screening methods, such as magnetic resonance imaging (MRI) that uses high magnetic field and radio waves, are also used. In MRI, patients are injected with gadolinium, a chemical dye that enhances the obtained image. However, this method has a higher rate of false screening than mammography [3] and does not determine the type of cancer cell lines.

Currently, Most of the detection methods are based on breast biopsies. The biopsy is examined by a pathologist under a microscope in order to look for cancerous cells. One or two weeks needed for the report to be completed.

### **1.2 Research Objectives**

This research aims to design a sensor to detect and differentiate the various types of cancer cell lines, such as breast cancer cells, based on their electrical properties (e.g., dielectric constant and conductivity). The three types of cancer cell lines, namely, MCF7, MDA-MB-231, and HS578T, will be examined. The electrical properties of these cancer cell lines were obtained from [4] and were evaluated through open-ended coaxial technique.

### **1.2.1 Sensor Characterization**

First, the sensor must have a compact size to make it handy and affordable. Second, the sensors' range of operation must be in ultra-high frequency (UHF) because high ranges will require an expensive machine for their readings. Moreover, with high frequencies, the conductor losses increase, thereby maximizing the chance of producing errors during readings. Third, the sensor must display a readout signal with a clear resonance for a user to differentiate various signals.

### **1.3 Overview**

The structural differences, such as the ratio of connective tissue to fat tissue, and the percentage of the intercellular fluids between cancerous and noncancerous biopsies contribute in defining the conductivity and permittivity of the cell lines [5]. Generally, malignant tumors have higher dielectric constant and conductivity than benign tumors [6]. Therefore, we can use the electrical properties of biopsies to diagnose whether a tumor is cancerous or noncancerous. In addition, we can classify the different types of cancer cell lines. Two near-field microwave techniques use the electrical properties of the material for sensing. The first technique is based on the reflection coefficient, and the second is based on the resonance frequency. The reflection coefficient can be obtained using two approaches, that is, measuring at the open end of a waveguide and a coaxial probe [7, 8].

The open-ended waveguide can be used for sensing application, as illustrated in Figure 1. Thus, the sample is placed in front of the waveguide and the shorting plate behind the sample. However, the waveguide method will be inapplicable to our case because the samples are too small, and this method is sensitive to noise.

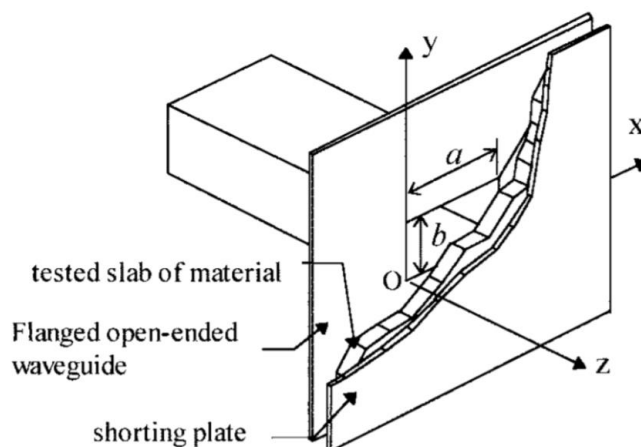


Figure 1: Open-ended waveguide for sensing application

The open-ended coaxial probe as shown in Figure 2 can be used for sensing by dipping the tip of the coaxial in the solution or by forcing the material to have full contact with the tip of the coaxial probe under test. This method will perform the required job, but its high-range operating frequencies will require an expensive vector network analyzer (VNA) that does not satisfy the requirements of the research.

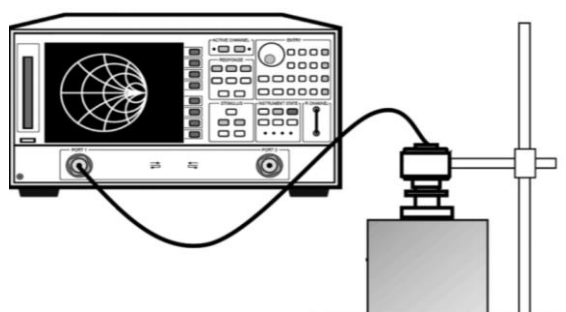


Figure 2: Open-ended coaxial probe for sensing application

Resonance frequency technique depends on the changes in the resonance frequency. This technique allows for control over the range of frequencies that can be used; thus, the designer can use low frequencies to reduce cost by using affordable VNAs. Moreover, the resonance frequency technique is generally more accurate than reflection coefficient-based technique [11].

### **1.3.1 Metamaterial**

A metamaterial is an engineered material that is composed of a combination of structures and materials. This material exhibits unique properties depending on the structure's orientation, dimension, shape, and base material. Its uniqueness comes from its negative electrical permittivity, magnetic permeability, and refractive index. The interest that the material gained has been due to its size compared with the affected electromagnetic waves because the target wavelength is larger than the size of the structural elements [12, 13]. In recent years, metamaterials have played an important role in sensing technology. Electromagnetic sensors use the changes that occur in the electromagnetic field when the transducer comes in contact with the material under test for sensing. The changes that arise in the fields lead to a shift in the resonance frequency along with changes in the amplitude of the response signal for a given port [14].

#### **1.3.1.1 Split Ring Resonators (SRRs)**

An SRR is a metamaterial structure, which can be modeled as an LC circuit that resonates at a frequency predetermined by the dimensions, material, and geometry of the structure. An SRR is a metallic loop with one or more small gaps. The loop can take many different shapes, circular, square, and hexagonal, as depicted in Figure 3 [15]. When a magnetic field passes through the ring, the field induces a current. The gap prevents the current from flowing, thereby increasing the resonance of the LC circuit. The resonance occurs when the capacitive reactance is equal to the inductive reactance in magnitude. Moreover, the gap acts as a capacitor, which allows the SRR to be used as a sensor. Any change in the material under test will cause a shift in the frequency. This feature can indicate the material type because each material has its

unique conductivity and dielectric constant [16]. SRRs are extensively used as sensors given their simplicity in designing, low relative cost, and ease of fabrication.

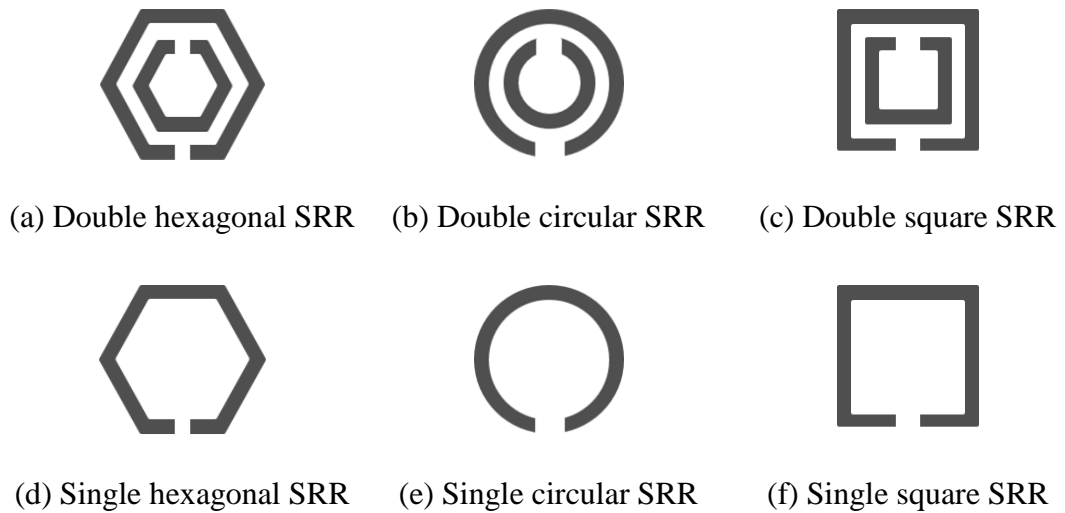


Figure 3: Split ring resonator designs

### 1.3.2 Fractal Hilbert Curve

Fractal designs are extensively used as antennas considering their ability to resonate at low frequencies while retaining their small size in contrast to the dipole antennas. Fractal structures can have a size of less than  $\frac{\lambda}{10}$  whereas the size of the dipole is approximately  $\frac{\lambda}{2}$  [17].

The Hilbert curve is a plane-filling curve according to David Hilbert in 1891 [18]. This curve is self-similar and its basic unit is U-shaped, as demonstrated in Figure 4. From the first order to the second order, the structure is reduced to half of its original size and is duplicated in three copies. Each corner point of the original unit becomes the center of the reduced sized structures, and then corner points are rotated. At the first point, the unit is rotated counter-clockwise by  $90^\circ$ . At the second and third points, the structures are retained without any rotation. At the fourth point, the unit is rotated clockwise by  $90^\circ$ . Similar steps can be repeated from the second order to the third

order and so on [19]. Three connecting segments are used to combine the four structures in each iteration.

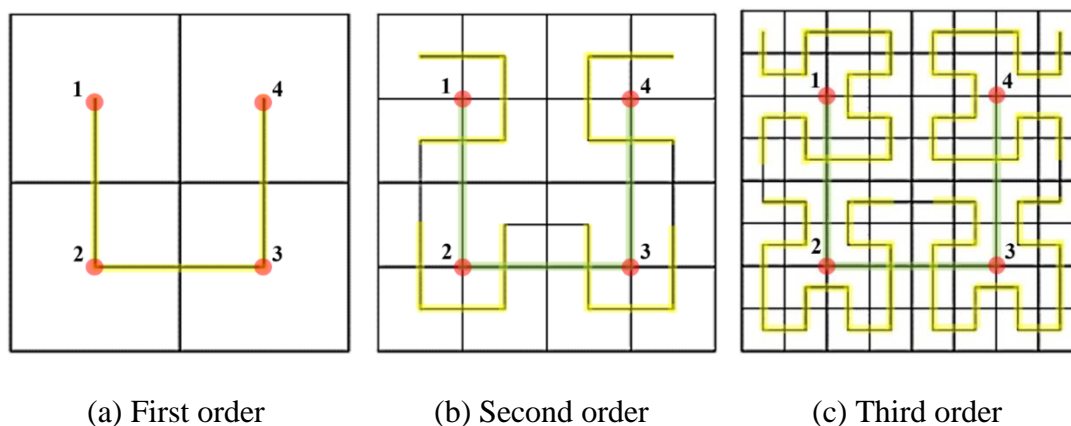


Figure 4: Hilbert curve

In the present research, the Hilbert curve will be used as a defected ground structure (DGS) to reduce the resonance frequency and increase the sensitivity of the sensor by enhancing the capacitance between the ground and the track [20]. DGS is a unit that is etched out from a metallic ground of a microwave printed circuit board (PCB). The etched out parts resonate depending on their shape and size. These parts are also used as band-stop and band-pass filters to control antenna harmonics and eliminate unanticipated surface wave [21].

### 1.3.3 Reflection and Transmission Coefficient

The relationship between input and output signals in an electrical system is presented by scattering parameters (S-parameters). The S-parameters represent the transmitted and reflected power. For a two-port system, the transmitted signal from Port 1 to Port 2 is expressed as  $S_{12}$ . Furthermore, the transmitted power from Port 2 to Port 1 is  $S_{21}$ . Moreover,  $S_{11}$  represents the power of the signal that was transmitted through Port 1 and reflected back to Port 1. Similarly,  $S_{22}$  is the reflected power that was transmitted through Port 2 and reflected back to Port 2.

### **1.3.4 High-Frequency Structure Simulator (HFSS)**

An HFSS is a 3D electromagnetic simulation program that is used to model, design, and simulate high-frequency electronic products. Its operating algorithm is based on applying numerical methods to solve electromagnetic-based models and calculate their resonance frequencies, S-parameters, impedances, and fields. This software is used extensively in designing antennas, filters, and PCBs [22]. In the present research, an HFSS will be used to design the sensor based on the mathematical model and simulate this sensor to ensure that it works correctly prior to fabrication.

### **1.3.5 Vector Network Analyzer (VNA)**

A VNA contains a signal generator and a receiver. A signal is applied to the device under test, and the receiver will acquire the response of such a signal on the system. Then, the original signal is compared with the received signal to measure the transmission, reflection parameters, and coefficients [23]. The VNA will be used to test the response of the sensor and verify the results obtained by the simulated design.

### **1.3.6 Electrical Properties of Cancer Cell Lines**

In the present research, we aim to detect and classify the types of breast cancer cell lines using their electrical properties, such as dielectric constant and conductivity. Three types of cancerous breast cell lines are used. The reference frequency is the resonance frequency of the vacuum. The electrical properties for different types of cancerous cell lines are obtained from the study of Jithin et al. [4] using the open-ended coaxial cable technique. The real part of the complex dielectric constant with respect to frequency is exhibited in Figure 5. In this figure, HS578-T, MCF-7, and MDA-MB-231 are malignant cell lines, and MCF-10A is a healthy cell line. The difference in permittivity between the healthy and malignant lines can be easily observed because the value of the dielectric constant of the cancerous cell lines exceeds 15 for a



frequency that ranges from 0 to 8 GHz, whereas for the normal cell line the dielectric constant falls below 5.

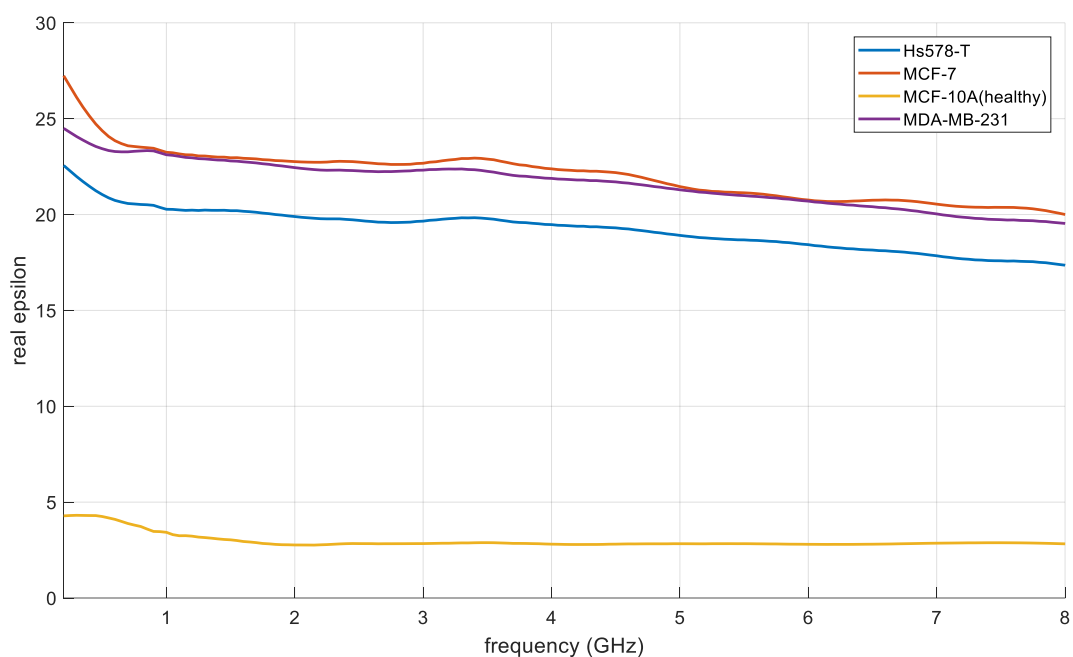


Figure 5: Real part of the complex dielectric constant with respect to frequency for different breast cell lines

Figure 6 presents the loss tangent of the cell lines with respect to frequency. The losses indicate dissipated energy and conductivity of the cell lines. Low frequencies yield few differences between the losses of healthy and cancerous cell lines. However, with the increase in the frequency, the losses increase at a higher rate in the cancerous cells than in the healthy cell lines.

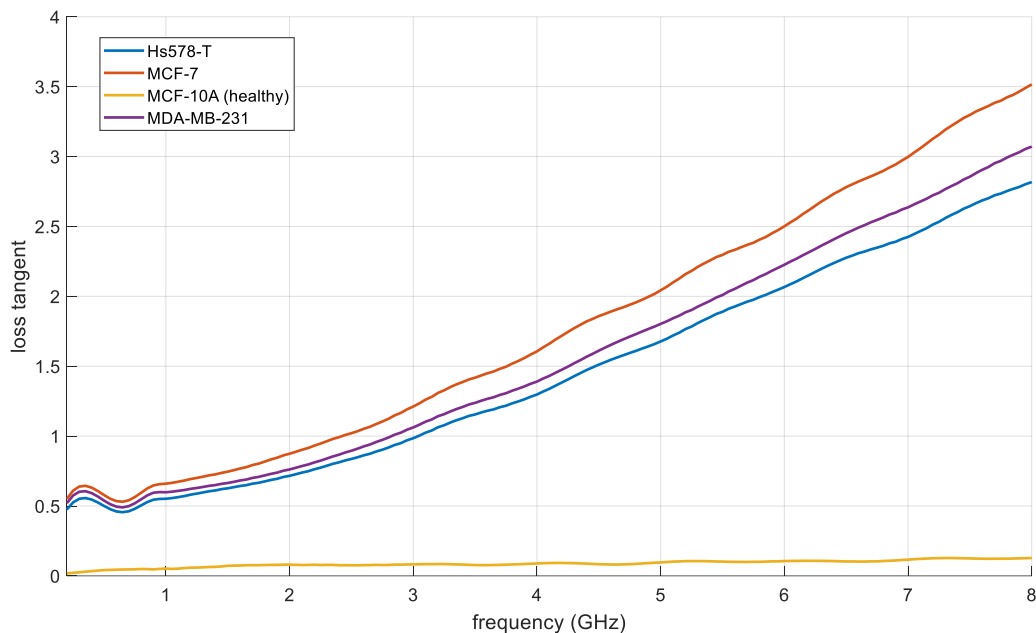


Figure 6: Tangent loss with respect to frequency for different breast cell lines

A low-range operating frequency, that is, lower than 3 GHz, is optimal because the resonance frequency increases with the losses of the microstrip. Moreover, using high-frequency ranges will require an expensive VNA with high-range operating frequencies, which does not satisfy the requirements of this research.

### 1.3.7 Different Defected Ground Topographies

During the designing stage, different orders of the Hilbert curve have been examined from the first order to the fourth order. High orders are not used because these orders will reduce the dimensions of the curve, which will not be obtained during fabrication considering the limited PCB etching machine. The first focus is selecting the order that yields the highest magnetic and electrical fields around the sample area to increase the capacitance and hence to increase the sensitivity of the sensor. The second focus is identifying the order that will provide the lowest operating frequency with the lowest reflection coefficient at the resonance frequency. The high magnetic and electrical fields can also be observed in the shift of the resonance frequency between the tested materials. If the fields are strong, then the capacitance of the sensor

will increase. Therefore, the sensitivity of the sensor will be high, thus leading to increasingly stable results. Figure 7 and Figure 8 display the magnetic and electrical fields, respectively. In these figures, the design with the fourth-order aperture Hilbert curve defected ground exhibits the strongest fields.

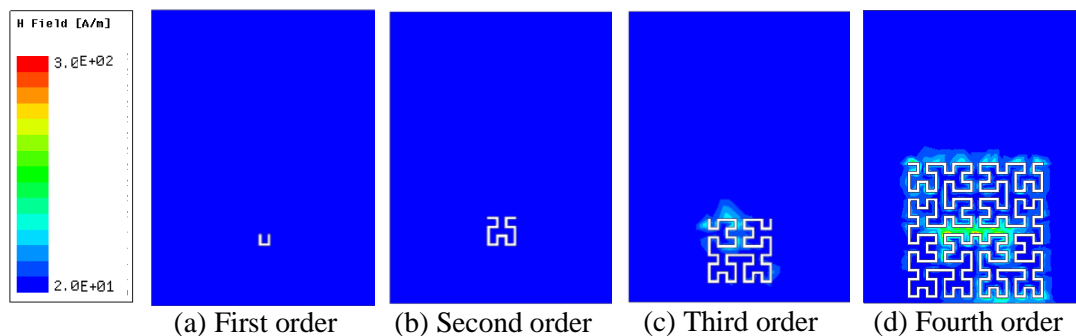


Figure 7: Magnetic field for different orders

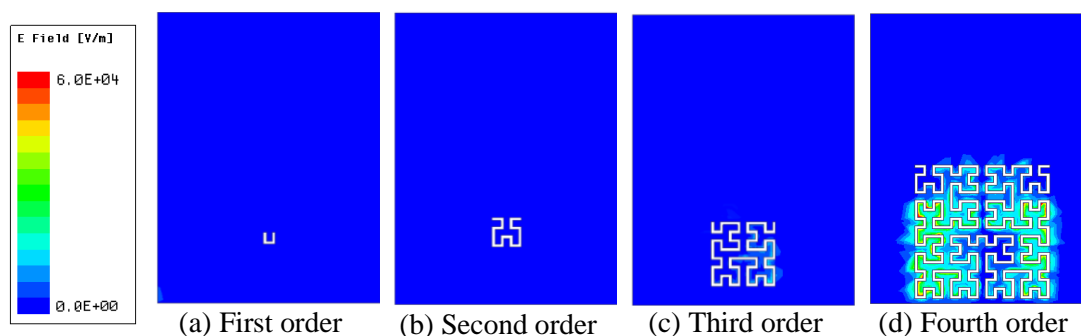


Figure 8: Electrical field for different orders

### 1.3.8 Support Vector Machine (SVM)

In machine learning, SVM, a type of supervised learning, uses a set of input-output pairs. SVM constructs a decision surface, that is, a hyperplane, which separates the data into two classes, thereby making SVM a binary learning machine. Thus, the distance between the two classes is maximized. SVM is used for classification and regression analysis. In this research, the SVM will be used to classify the cancerous cell types.

## Chapter 2: Literature Review

In recent years, new techniques and sensors have been developed to detect and classify different types of cancerous cells based on their physical, chemical, and electrical properties. In 2014, Atif et al. [24] studied malignant and benign tumors based on their spectral features. The samples were exposed to multiple beams of ultraviolet light to excite them in emitting light as presented in Figure 9. The differences between the position of the maximum band absorption and emission of each beam were considered. The experiment showed a vertical shift relative to the fluorescence intensity, thereby indicating that the tested cancerous cells had higher relative fluorescence intensity, thereby indicating that the tested cancerous cells had higher relative fluorescence intensity than non-cancerous cells. This result was due to the differences in their bimolecular structures. Using the same concept, in 2016, Kimura et al. [25] developed a device that detects cancer by monitoring mutated micro-ribonucleic acid (miRNA). The miRNA was collected from a blood sample. Then, a complementary deoxyribonucleic acid (DNA) was synthesized from the miRNA. Subsequently, the complementary strands were monitored using a quantitative polymerase chain reaction by intercalating fluorescent reagents and measuring the intensity of its fluorescence with a photodiode, such that the emission intensity is expressed in the changes in the voltage level.

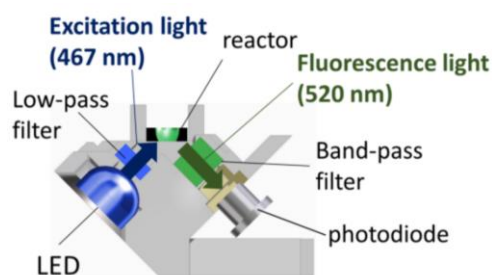


Figure 9: Structure of the optical system module

In 2016, Ali et al. [26] used micropores to differentiate cancerous and healthy cells. The size was designed to be smaller in the pore than in both cell types to test

their elasticity. Cancerous cells have higher elasticity than normal cells given their high percentage of fluids. The passing time of the cells to the micropore was recorded along with the current across the pore. Cancerous cells had lower blockage incidences and took less time to pass the pore than healthy cells. Moreover, cancerous cells showed less current blockage than healthy cells.

In recent years, metamaterial-based transducers have been well known considering their strong electrical and magnetic fields, high sensitivity, compact size, and low fabrication cost. The advantages of microwave sensors to these transducers have gained a special interest in the biomedical field and structural analysis. I. Rusni and A. Ismail [27] used metamaterials to design a sensor that detects DNA hybridization. Multiple SRR structures were utilized to enhance the localization field of the sensor as presented in Figure 10. Consequently, the sensitivity would be improved because the detection mechanism is based on the resultant shift in the resonance frequency that occurs due to the interactions of the samples with the electrical field of the sensor. These researchers used single-stranded and complementary DNAs at different concentrations. The sensitivity of the sensor is 10 MHz/ $\mu$ Mole for an operating frequency of 4.96 GHz [27]. Similarly, H. Lee et al [28] designed a double SRR as shown in Figure 11 to detect the hybridization of single-stranded DNA with complementary DNA. These authors found that adding gold on the surface of the sensor increases the obtained shift from 20 MHz to 60 MHz [28].

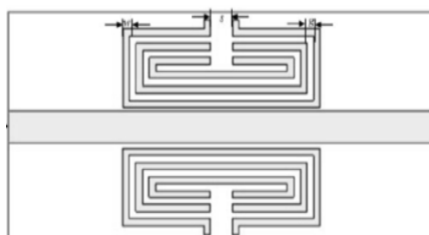


Figure 10: Multi split ring resonator sensor

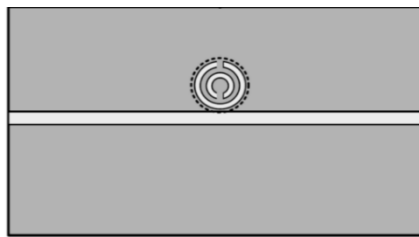


Figure 11: Double split ring resonator sensor

SRRs are used to observe the healing process of fractured bones. Melik et al. [29] implemented a wireless transducer that measures the strain during the healing process of a fractured bone. The concept of operation depends on the effect of a mechanical load on the resonance frequency. Any applied mechanical strain will cause deformation in the structure, thus causing a shift in the resonance frequency. These researchers compared two structures, namely, classical as shown in Figure 12 and nested metamaterials as presented in Figure 13. The increased number of gaps in the nested structure demonstrated an advantage in increasing the sensitivity from 1.09 kHz/kgf to 0.72 kHz/kgf [29].

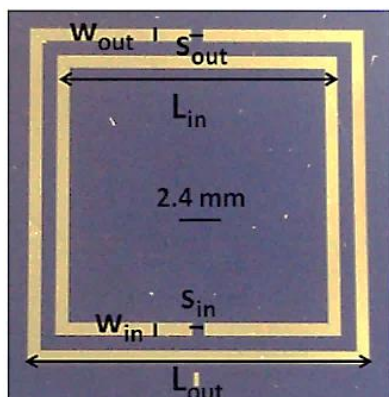


Figure 12: Classical structure

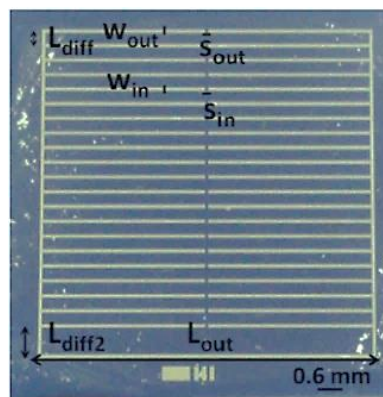


Figure 13: Nested structure

Similarly, Li, Withayachumnankul, Chang, and Abbott [30] designed two transducers to measure mechanical strain. These authors used two metamaterial structures, namely, I and crossed-I as presented in Figure 14 and Figure 15 respectively. The principle of operation depends on the effect of the gap's dimensions on the resonance frequency. When the gap decreases, the capacitance increases,

thereby leading to a shift in the resonance frequency. The I-shaped transducer can work effectively on only one axis. By contrast, the crossed I-shaped transducer can describe deformation along two axes independently. Moreover, the maximum sensitivity for the two sensors is  $107 \text{ GHz}/\mu\text{m}$  [30].

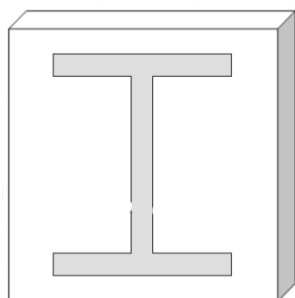


Figure 14: I-shaped structure

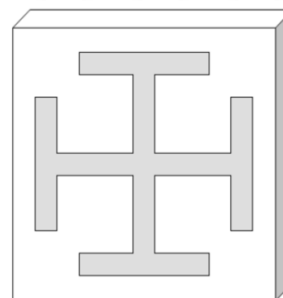


Figure 15: Crossed-I shaped structure

Microwave sensors have also been used to diagnose cancer. Spada, Bilotti, and Vegni [31] designed a metamaterial-based biosensor to distinguish a malignant tumor from a benign tumor. The working principle of the sensor depends on the dielectric constant and the absorption value of each tumor type. Thus, the change in amplitude and shift in frequency of the S-parameters would indicate the presence of cancerous cells. The sensor was formed using the complementary omega particle structure as shown in Figure 16, and the material under test should be placed behind the structure. The obtained results showed a successful difference between cancerous and non-cancerous tumors [31].

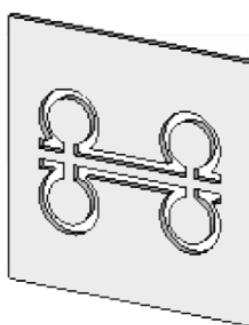


Figure 16: Multi-SRR sensor

Similarly, M. Asad et al [32] designed a transducer using double SRR structures as presented in Figure 17 to detect different types of biological tissue. When they placed the material at the SRR's gap, a shift in resonance frequency was observed in the reflection coefficient phase. Each material had its own amount of shift, thereby allowing the researchers to differentiate materials based on the obtained shift [32].

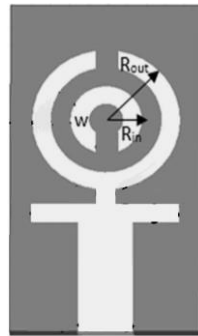


Figure 17: Double SRR sensor

Moreover, Hardinata et al. designed two microwave sensors using square and circular complementary SRR (CSRR) structures that operate at a frequency of 2.4 GHz, as displayed in Figure 18. The sensing mechanism depends on the shift of the resonance frequency and the changes in the quality factor by placing different biological tissues. During the experiment, a problem occurred when measuring biological samples that contained blood. The measurements did not match the simulated results, and the sensitivity of the sensor was lost. However, the problem was solved by adding water-resistant tape that made the sensor responsive at a thickness that reached 6 mm of the tested material [33].



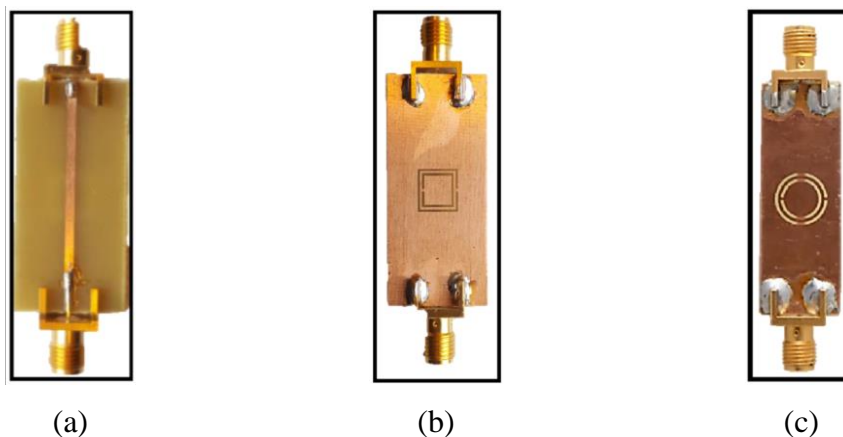


Figure 18: Transducer layout (a) Top view (b) Bottom view of square CSRR (c) Bottom view of circular CSRR

Additionally, a research was done by A. Alghamdi and S. Mohammadi [34] in which they designed a label-free RF sensor to detect a single cell and characterize it. The design consists of two circular split ring resonators, a dry cell should be placed at one of the gaps and the response of the transmission coefficient is observed. In order to remove the watery content, the team used an evaporation technique. The sensor is designed to operate at a frequency of 2 GHz, when a healthy cell (HaCaT) was placed at one of the gaps while keeping the other gap unloaded, a downshift of 0.03 GHz and an increase of 1.1 dB occurred. However, when a cancerous cell (Glial) was placed at the gap while keeping the other gap unloaded, a downshift of 0.02 GHz and a decrease of 0.6 dB occurred [34].

Some researchers have used microwave sensors as an alternative to glucose-oxidation-based sensors in glucose meters. Niloofar, Mohammad, and Mojgan [35] designed three transducer topographies and investigated their sensitivity. The three designs were rotated versions of each other and coupled with a microstrip transmission line, which had a gap in the middle, as illustrated in Figure 19. The main design consisted of a rectangular SRR with an inwardly curved gap that was aligned with the gap in the transmission line. The intended application is to examine the frequency

response of the sensor with respect to different glucose concentrations. These researchers found that, when the gaps are aligned, the sensitivity is the highest because the variations in the amplitude become increasingly noticeable [35].



Figure 19: Three transducer topographies

Furthermore, Supakorn, Urit, and Anuwat designed a tapped circular SRR to observe the relationship between the transmission coefficient and glucose concentrations. The samples were placed on the gap to cover the circle tap as shown in Figure 20. The results showed that the transducer can detect the changes in glucose concentration from 0.12 g/mL and above because the shift in the transmission coefficient is apparent [36].

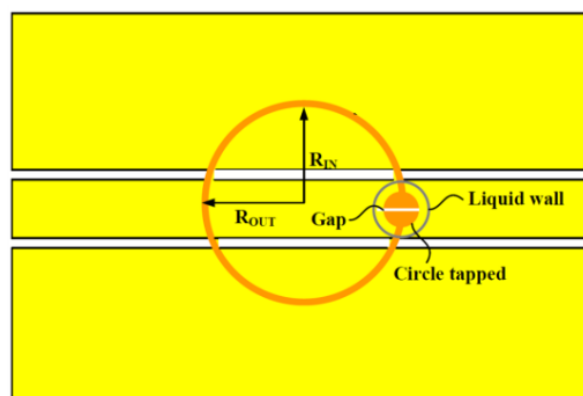


Figure 20: Tapped circular SRR

Microwave sensors have been applied to detect cracks in metallic structures, such as aircraft and steel bridges. The use of these sensors has an advantage over other methods given the ability of the sensor waves to penetrate the material, thereby eliminating the requirement for surface cleaning and any coat removal. In Figure 21,

Ali and Omar designed a CSRR-based sensor to detect cracks in an aluminum block because the cracks cause a disturbance in the electromagnetic field that shifts the resonance frequency. The sensor was tested in different orientations and can only detect cracks by scanning in the y-direction such that the movement is perpendicular to the crack. Moreover, two studies were conducted using an HFSS. The first study was realized when the researchers fixed the width of the crack to 0.2 mm and varied the depth and then found that the shift in the resonance frequency decreases with the increase in the crack depth. The second study was fulfilled when they fixed the depth to 2 mm and varied the width and then observed that the shift in the transmission coefficient increased with the crack width. After fabrication, Ali and Omar tested the sensor for a crack with width and depth of 0.2 and 2 mm, respectively. The results yielded a shift of 1.8 GHz [7].

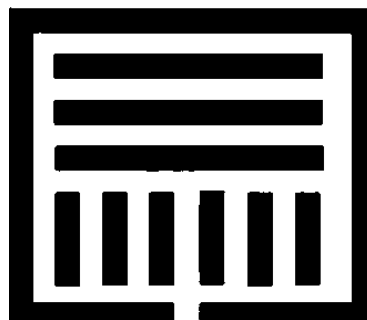


Figure 21: Sensor layout, the black areas are the etched out regions, and the white areas are the conductor

Similarly, Taehwa and Sungjoon designed a CSRR sensor that is incorporated with a substrate-integrated waveguide (SIW) for crack detection, as depicted in Figure 22. The SIW was used to achieve high power capacity, such that the transducer would be sensitive to the effective capacitance of the sensor and material under test, thus leading to a legible shift in the resonance frequency. The sensor was coated with a layer of Teflon to reduce the impedance mismatch between the sensor and the material under test. Moreover, an aluminum block, with crack width ranging from 0.1 mm to 2

mm for two cases, with crack depths of 1 and 2 mm, was used in testing the sensor. The resonance frequency of approximately 5 GHz of the block without cracks was used as a reference. The maximum and minimum observed shifts in the case with a crack depth of 1 mm are 220 and 2.25 GHz/m, correspondingly. Furthermore, the maximum and minimum shifts in the case with a crack depth of 2 mm are 280 and 2.5 GHz/m, respectively [37].

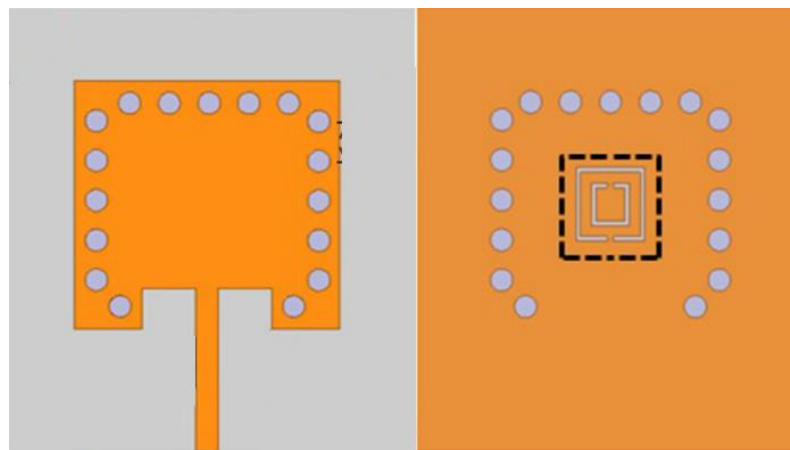


Figure 22: CSRR-loaded SIW cavity

The Hilbert curve described in Section 1.3.2 has been used recently in different applications, such as in wireless applications. D. Kim, C. Kim and D. Yang [38] designed an omnidirectional antenna using a flexible Hilbert curve loop for the WLAN/WiMAX communication system. These authors investigated the performance of a triple-band antenna when a rectangular loop is substituted with a third-order Hilbert curve loop, as demonstrated in Figure 23. These researchers observed favorable far-field characteristics, antenna factor, and circular polarization performance. Moreover, the area was twice smaller in the Hilbert loop than in the rectangular loop given its space-filling property, whereas both of the designs exhibited the same operation bands.



Figure 23: Flexible Hilbert curve loop antenna

Similarly, Karmakar et al. [39] designed an ultra-wide band antenna with a perturbed Hilbert slot for WLAN, WiMAX, and C-band application. The Hilbert curve was used to create a multi-band rejection. Moreover, these researchers outlined the effect of adding fractal shapes on antennas' characteristics by improving the radiation characteristics and providing an ultra-wide bandwidth that corresponds to its space-filling property. Furthermore, they presented the effect of adding a perturbed fractal slot on antennas' response and the method through which perturbed fractal slot creates a multi-band notch.

The Hilbert curve has also been used in designing sensors. Radonić, Kitić and Crnojević-Bengin adopted the Hilbert curve to design a soil moisture sensor, as presented in Figure 24 [40]. The working principle of the sensor depends on the phase shift of the signal with respect to the different levels of soil moisture. In addition, these researchers used a Hilbert fractal curve to increase the inductance of the sensor without increasing the sensor's size, thus increasing the sensitivity of the transducer. The operating frequency of the sensor was 1.2 GHz with a phase shift range of  $66.64^\circ$  and an insertion loss of 2.98 dB. To further increase the range of the phase shift, a partial ground, rather than a full ground, was utilized. This change resulted in an increase in the range from  $66.64^\circ$  to  $70.76^\circ$ .

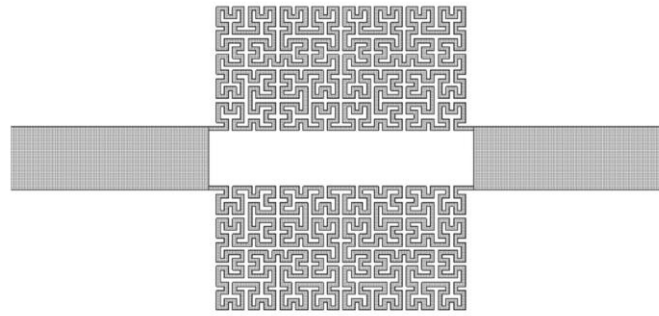


Figure 24: Hilbert curve used in designing a soil moisture sensor

In another study, Khayam and Alfaruq used the Hilbert curve to design an antenna for detecting partial discharges in high-voltage equipment [41]. The target range was from 300 MHz to 3 GHz. These researchers focused on the feeding location, the material of the substrate and its thickness, and their effect on the frequency response of the antenna. Similarly, Darmawan and Khayam investigated the effect of the order of the Hilbert curve for partial discharge detection along with the antenna size [42]. Six antennas were studied. The first three antennas had a size of  $7 \text{ cm} \times 7 \text{ cm}$  with a Hilbert curve of the orders 2, 3, and 4. The second three antennas had a size of  $10.5 \text{ cm} \times 10.5 \text{ cm}$  with the same orders as the first three antennas. Thus, with orders higher than 1, the antenna starts having a wide bandwidth. Moreover, the resonance frequency decreases with the increase in size. Similarly, Harbaji et al. [43] used a fourth-order Hilbert fractal curve in designing a wideband antenna to detect different types of partial discharges that occur in an oil-paper insulated system, as displayed in Figure 25. The types that were examined were surface discharge, sharp edge to a ground plane, and void in insulation discharge. Each type exhibited a variation in the obtained frequency. The acquired frequency samples were classified into their corresponding types using pattern recognition. The surface discharges had frequencies in the whole captured range and lasted simultaneously. This discharge caused inconvenience to the researchers given the misclassification of other types. Moreover, the response of the sharp point appeared between 1.8 and 2.2 GHz. Furthermore, the

void in insulation showed a response in a low-frequency range of approximately 100 MHz. K-nearest neighbor (KNN) and ANN for partial discharge classification were used. A recognition rate of 95% was achieved using the KNN, and a rate of more than 93% was obtained using the ANN under different conditions.

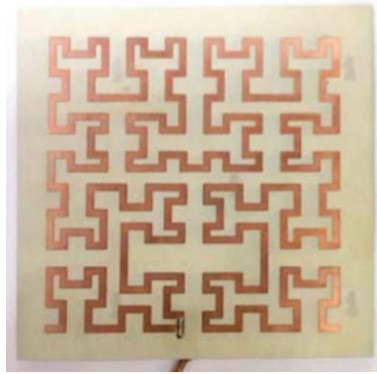


Figure 25: Fabricated Hilbert antenna

## Chapter 3: Design Methods and Analysis

The sensor consists of an SRR with a perturbed Hilbert curve as a DGS as presented in Figure 26. The sensor feed was designed by coupling a microstrip transmission line with the SRR. The space between the transmission line and the gap of the SRR must be the location of the sample. In this section, different topographies of the sensor will be studied. Moreover, the mathematical model of the sensor will be investigated along with the simulated model.

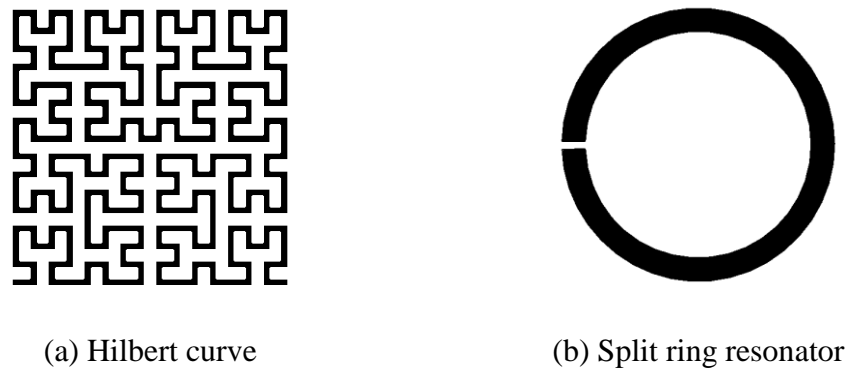


Figure 26: Structures used in the design

### 3.1 Theoretical Model and Design

#### 3.1.1 SRR

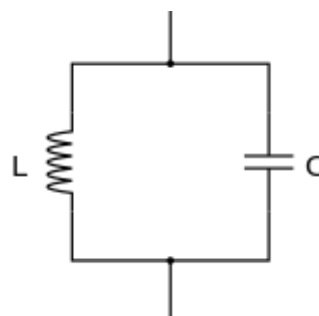


Figure 27: LC circuit

The sensor is designed to operate at a frequency of 15.4 GHz and it must be of a compact size for ease of usability. Considering that the size is inversely proportional to the frequency, the resonance frequency resulted in the high-frequency range. The



circuit model of the SRR is presented in Figure 27. The resonance frequency for the SRR can be obtained using the equation of an LC circuit [44].

$$f = \frac{1}{2\pi\sqrt{LC}} \quad (1)$$

The inductance of the resonator can be obtained using the following equation [44]:

$$L = \mu_0 R_m \left( \ln \left( \frac{8R_m}{h+w} \right) - 0.5 \right) \quad (2)$$

where  $\mu_0$  is the free space permeability,  $h$  is the height of the ring,  $w$  is the width of the ring, and  $R_m$  is the mean radius.  $R_m$  is calculated using Eq. (3).

$$R_m = R + \frac{w}{2} \quad (3)$$

Where  $R$  is the radius of the SRR. The total capacitance,  $C$ , of the split ring resulted from the parallel combination of the gap and surface capacitance, as expressed in Eq. (4).

$$C = C_{\text{gap}} + C_{\text{surf}}, \quad (4)$$

where  $C_{\text{gap}}$  is the capacitance of the gap and can be calculated using Eq. (5).  $C_{\text{surf}}$  is the capacitance of the ring surface and can be calculated using Eq. (6) [45].

$$C_{\text{gap}} = \varepsilon_0 \left| \frac{wh}{g} + \frac{2\pi h}{\ln\left(\frac{2.4h}{w}\right)} \right| \quad (5)$$

$$C_{\text{surf}} = \frac{2h\varepsilon}{\pi} \ln\left(\frac{4R}{g}\right) \quad (6)$$

In Eq. (5),  $g$  is the length of the gap,  $\varepsilon_0$  is the permittivity of the free space, and  $\varepsilon$  is the permittivity of the substrate.  $\varepsilon$  can be expressed as

$$\varepsilon = \varepsilon_0 \varepsilon_r, \quad (7)$$

where  $\epsilon_r$  is the relative permittivity of the substrate. Table 1 lists the values of parameters used in Eqs. (2), (3), (5), and (6) for the proposed SRR resonance frequency calculation.

Table 1: Parameters used to design the SRR

$g$	$R$	$w$	$h$	$\mu_0$	$\epsilon_0$	$\epsilon$	$\epsilon_r$
0.5 mm	8 mm	1.5 mm	0.035 mm	$1.2 \times 10^{-7}$ H/m	$8.85 \times 10^{-12}$ F/m	$3.26 \times 10^{-11}$ F/m	3.68

### 3.1.2 Perturbed Hilbert Ground

To reduce the resonance frequency of the SRR and increase the sensitivity of the sensor, we added the Hilbert curve, which was discussed in Section 1.3.2, as a DGS. The following approximation was used to obtain the resonance frequency of the defected ground [38]:

$$f_{\text{DGS}} \approx \frac{C_0}{2S_s\sqrt{\epsilon_r}}, \quad (8)$$

where  $C_0$  is the speed of light,  $\epsilon_r$  is the permittivity of the medium that surrounds the defected ground structure, in this case it is vacuum and it is equal to 1, and  $S_s$  is the length of the perturbed Hilbert curve slot.

$$S_s = (2^n + 1)l_s, \quad (9)$$

where  $n$  is the curve order, and  $l_s$  is the side length of the curve, as illustrated in Figure 28. Table 2 shows the values that were used to design the Hilbert curve.

Table 2: Parameters used to design the Hilbert curve

$l_s$	$S_s$	$n$
11.5 mm	195.5 mm	4

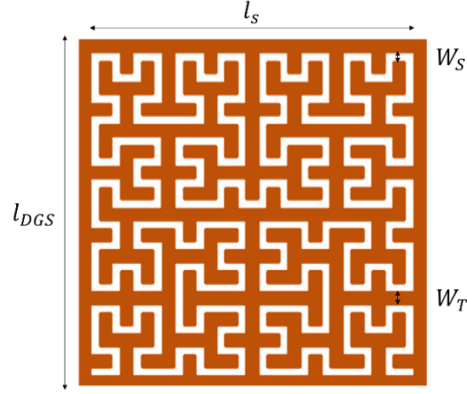


Figure 28: Perturbed Hilbert curve

In Eqs. (8) and (9), the perturbed Hilbert curve resonates at a frequency of 0.767 GHz.

### 3.1.3 Combined Design

To obtain the resonance frequency of the combined design, the total capacitance and inductance must be obtained. The capacitance of the split ring can be calculated using Eq. (4), and the inductance can be found using Eq. (2). To find the inductance of the perturbed Hilbert curve under the condition of  $\left(\frac{W_T}{H}\right) < 1$ , where  $H$  is the thickness of the substrate, and  $W_T$  is the width of the metal track of the DGS, the inductance of the DGS can be approximated as follows [46]:

$$L_{DGS} = \frac{60S_T}{c_0} \ln\left(\frac{8H}{W_T} + \frac{W_T}{4H}\right), \quad (10)$$

where  $S_T$  is the length of the metal track of the DGS. This variable can be obtained using Eq. (11).

$$S_T = \frac{l_{DGS}^2 - W_S l_s (2^n + 1)}{W_T}, \quad (11)$$

where  $l_{DGS}$  is the side length of the DGS, and  $W_S$  is the width of the slot, as depicted in Figure 28. Table 3 lists the values used for designing the DGS.

Table 3: Parameters used to design the perturbed Hilbert curve

$H$	$W_T$	$W_S$	$S_T$
1.6 mm	0.5 mm	0.25 mm	214.75

Accordingly, the value of the inductance is used to obtain the capacitance of the perturbed Hilbert curve.

$$C_{DGS} = \frac{1}{4\pi^2 L_{DGS} f_{DGS}^2} \quad (12)$$

The combined SRRs and DGS are parallel; thus, the total capacitance of the design is equal to the parallel combination of the split ring capacitance and the perturbed Hilbert curve capacitance, as demonstrated in Figure 29. The capacitance of the SRR and DGS are 0.00327 and 0.30866 pF, correspondingly. The total capacitance is 0.31193 pF. Similarly, the total inductance is equivalent to the parallel combination of the split ring inductance and the perturbed Hilbert curve induction. The SRR and DGS inductances are 0.032475 and 0.30866  $\mu\text{H}$ , respectively. The equivalent inductance is 0.026343  $\mu\text{H}$ .

Finally, the equation of the LC circuit must be used to acquire the resonance frequency of the entire design, as exhibited in Eq. (1). Subsequently, the design resonates at a frequency of 1.756 GHz.

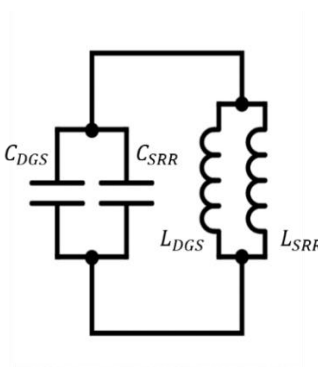


Figure 29: Equivalent circuit of the SRR and the DGS

## 3.2 Simulated Model

### 3.2.1 SRR

The HFSS was used to design and simulate the unit cell, as displayed in Figure 30. The parameters that were provided in the theoretical model described in Section 3.1.1 were used to simulate the SRR. In Figure 31, the unit cell resonates at a frequency

of 15.4 GHz, which is the same frequency obtained using the mathematical model of the SRR in the previous section. Figure 32 illustrates the boundary conditions along with the excitation ports used in the HFSS to simulate the unit cell.

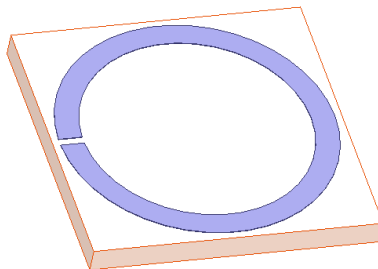


Figure 30: SRR unit cell

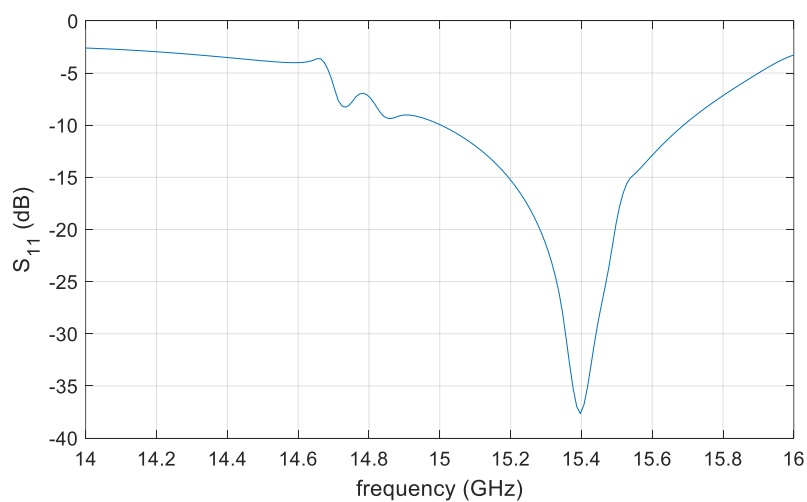
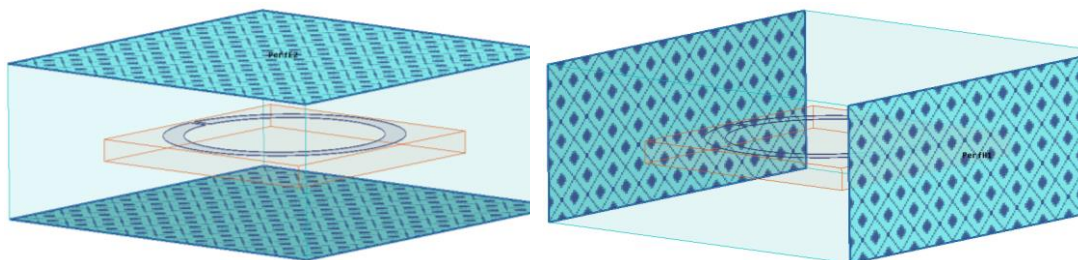


Figure 31: Simulated reflection coefficient of the SRR



(a) E-field

(b) H-field

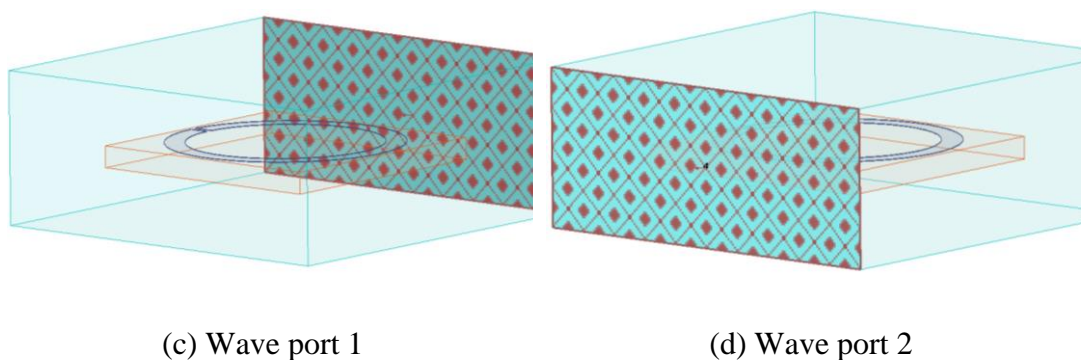


Figure 32: SRR unit cell simulation

### 3.2.2 Perturbed Hilbert Curve

#### 3.2.2.2 Fourth-Order Perturbed Hilbert Curve

To verify the obtained results from the mathematical model, the design of the perturbed Hilbert curve was simulated using the HFSS as a unit cell, as presented in Figure 28. The unit cell simulation resulted in a resonance frequency of 0.751 GHz as illustrated in Figure 33. The result of the simulation supports the obtained result from the approximation with a percentage difference of 2.09%.

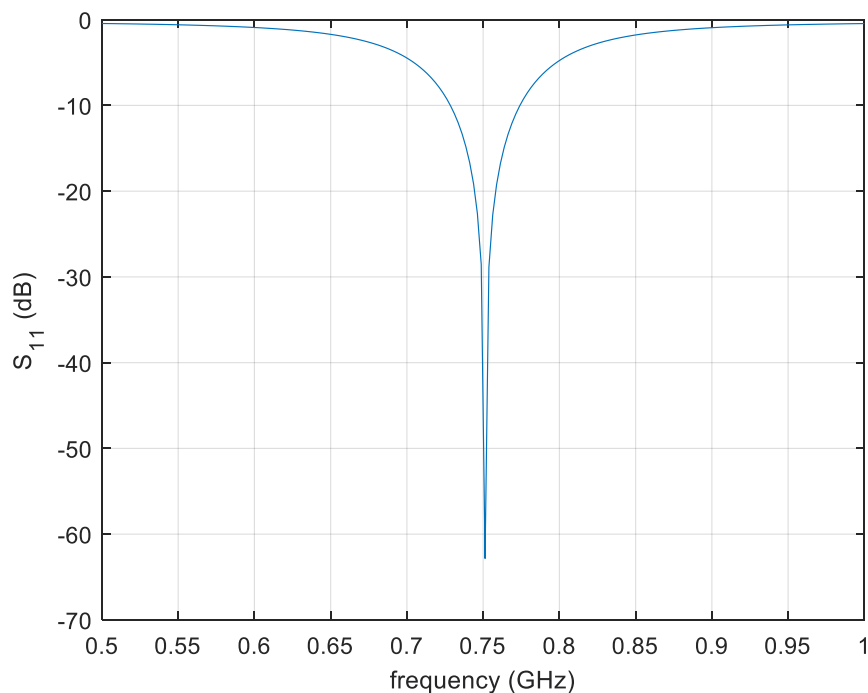


Figure 33: Simulated reflection coefficient of the DGS

### 3.2.3 Combined Design

In this section, the SRR and the perturbed fourth-order Hilbert ground are combined to yield the complete optimal design. The final design was excited using a two-port microstrip transmission line as shown in Figure 34. The model was simulated using the HFSS, and its reflection coefficient was obtained to reaffirm the value of the resonance frequency that was obtained using the theoretical model in Section 3.1.3.

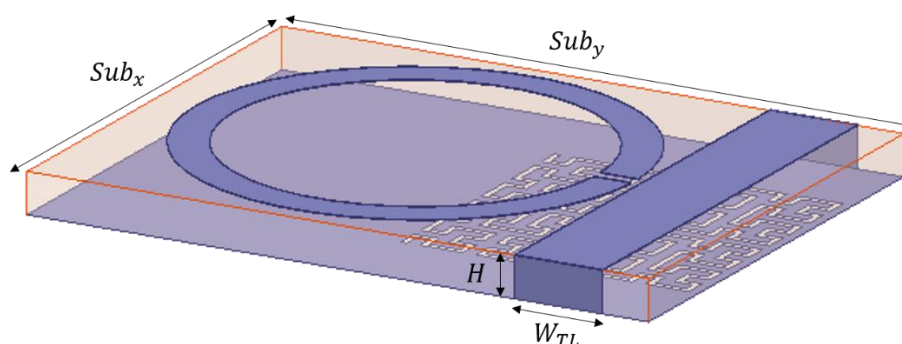


Figure 34: Sensor design

The split ring was placed on a substrate with a width of  $Sub_x = 19$  mm and a length of  $Sub_y = 28.8$  mm. The transmission line has the same length as the substrates and has a width of  $W_{TL} = 3.5$  mm. These parameters resulted in an input impedance of  $50.15 \Omega$ , which approximately matches the impedance of the coaxial probe and an electrical length of  $68.32^\circ$ . The sensor was excited through two ports, one at each end of the transmission line. After simulation, the resonance frequency was 1.778 GHz, as depicted in Figure 35. The percentage difference between the simulated and calculated resonance frequencies is 1.24%.

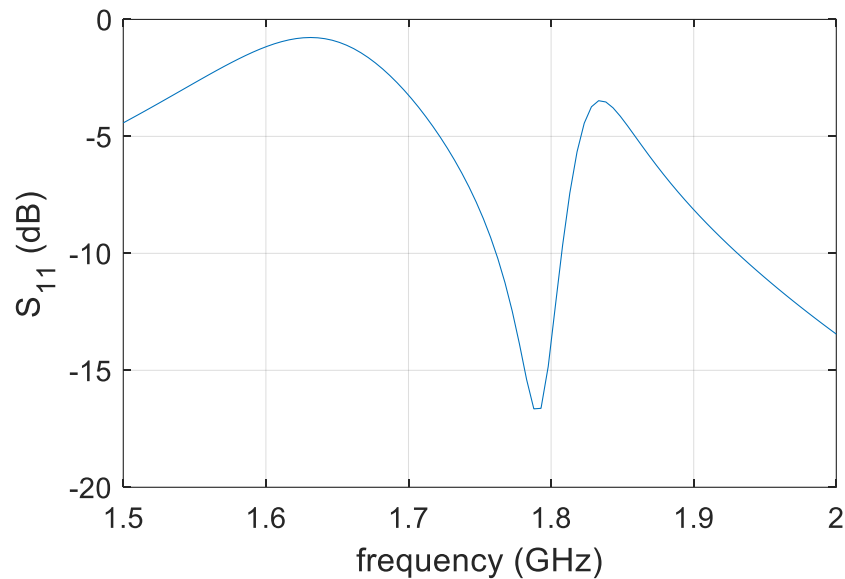


Figure 35: Simulated reflection coefficient of the final design

To study the range of the resonance frequencies and its response with the different test samples, we used four designs of different orders of Hilbert curve similar to that of Section 1.3.7 along with the design of a complete ground. Each design was simulated for vacuum, healthy MCF tissue, and cancerous MCF tissue. In Figure 36, the scattering parameter  $S_{12}$  of the five designs, that is, first-, second-, third-, and fourth-order Hilbert curves, and without any DGS, were observed, that is, the order of the fractal ground increases with the decrease in the resonance frequency. Furthermore, the transmission improves by increasing the fractal order. Therefore, the fourth order was selected because its low resonance frequency will reduce the conductor losses, thus decreasing the error that could occur. Moreover, given that the transmission is optimal when using the fourth order, the results are expected to be stable and thus will be less affected by system disturbances.



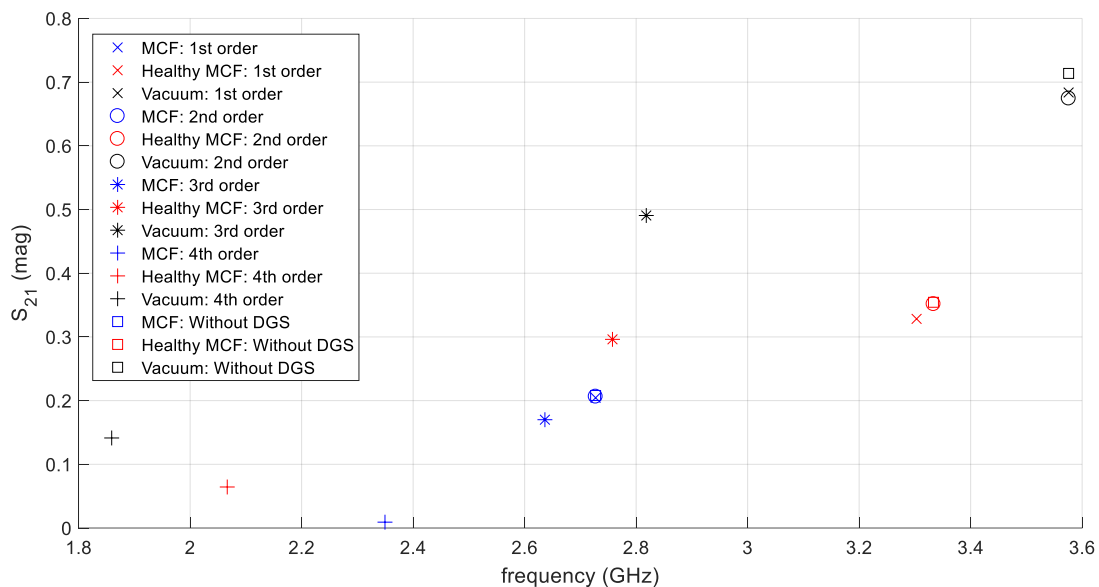


Figure 36:  $S_{21}$  of the SRR with different aperture Hilbert curve orders

### 3.3 Simulated Response of the Sensor

In this section, the model shown in Figure 37 of the sensor, which was presented in Section 3.2.3, was used to simulate its response when placing different cell types. The electrical properties of cell lines, which were described in Section 1.3.6, are used to simulate the cancer cells using the HFSS.

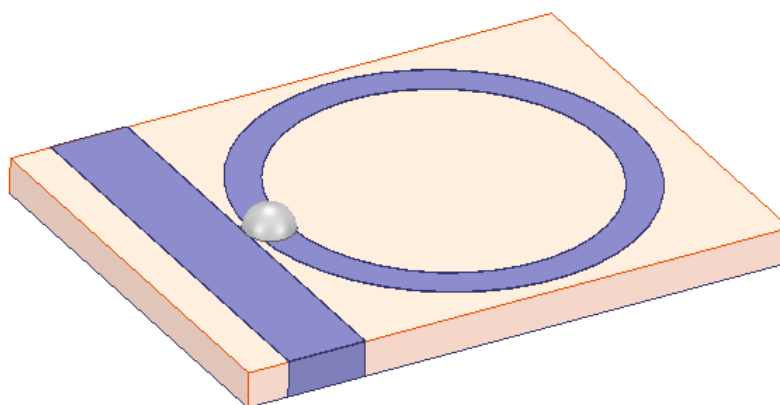


Figure 37: Sensor model with a sample of a cancer cell line

The breast cancer cell was simulated as a hemispherical shape that has a radius of 1 mm and was placed such that it covers the gap of the SRR. Moreover, the cell was enclosed within an air box such that the distance between the edge of the substrate and

the box is  $\frac{\lambda}{4}$ , as suggested by the HFSS supplier. The wavelength can be calculated using Eq. (13).  $f$  is the resonance frequency of the sensor.

$$\lambda = \frac{c}{f} \quad (13)$$

During the simulation, variations are clear when looking through the transmission coefficient, rather than the reflection coefficient. The transmission coefficients for vacuum, MDA-MB-231, MCF-7, and HS578-T, are displayed in Figs. 38 and 39 in magnitude and degree angles.

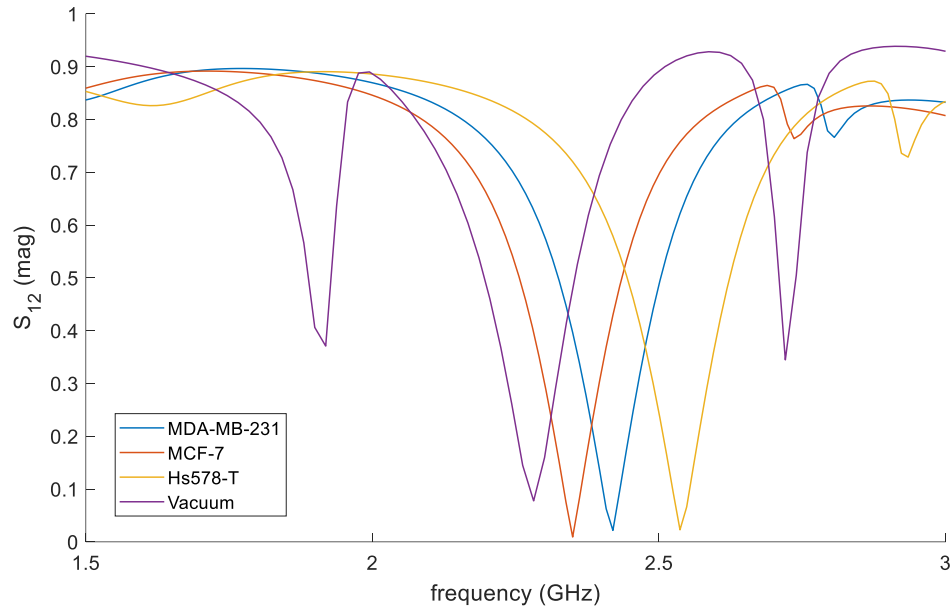


Figure 38: Simulated  $S_{12}$  in magnitude

Figure 38 displays the transmission coefficient in magnitude. The MCF-7, MDA-MB-231, and MDA-MB-231 cell lines show a resonance of 2.349, 2.42, and 2.537 GHz, correspondingly. The vacuum is regarded as a reference point. When nothing is placed in the gap, a resonance frequency of 2.281 GHz in the transmission coefficient exist. Thus, the minimum shift among the three types is 71 MHz. Similarly, Figure 39 plots the transmission coefficient in degree angle. Table 4 summarizes a comparison of the shift in frequency with respect to the resonance frequency of the vacuum, as defined in Eq. (14).

$$\Delta f = f_{cancerous\ cell} - f_{vacuum} \quad (14)$$

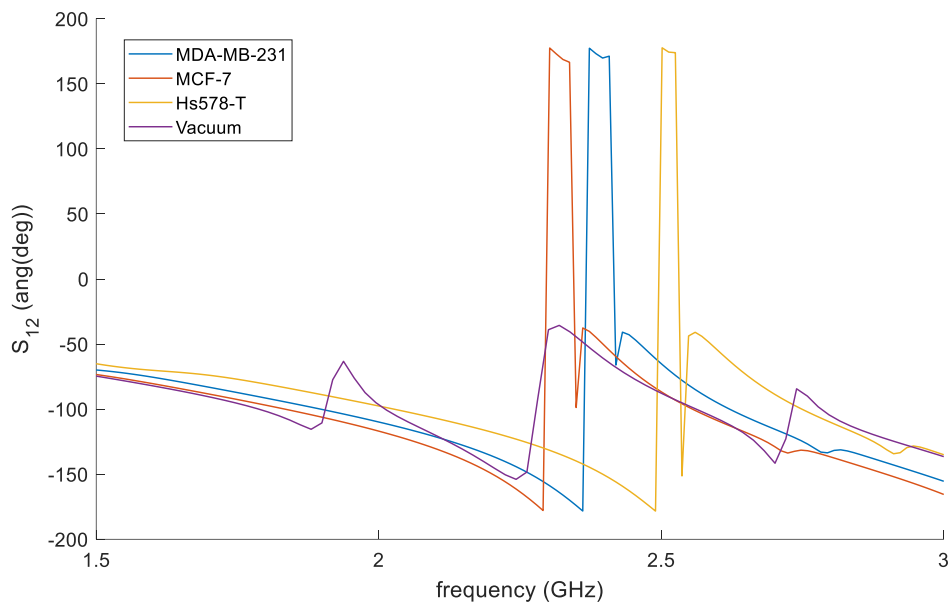


Figure 39: Simulated  $S_{12}$  in degree angle

Table 4: Shift in frequency with respect to the vacuum's resonance frequency

	<b>MDA-MB-231</b>	<b>MCF-7</b>	<b>HS578-T</b>
<b>Shift with respect to the vacuum (<math>\Delta f</math>)</b>	139 MHz	68 MHz	256 MHz

## Chapter 4: Results and Discussion

In this chapter, the sensor, which was discussed and designed in Chapter 3 is fabricated and tested using different types of breast cancer cell lines. Figure 40 presents a schematic of the measurement setup. The response of different cancer cell lines will be generated and compared with the results obtained from the simulation.

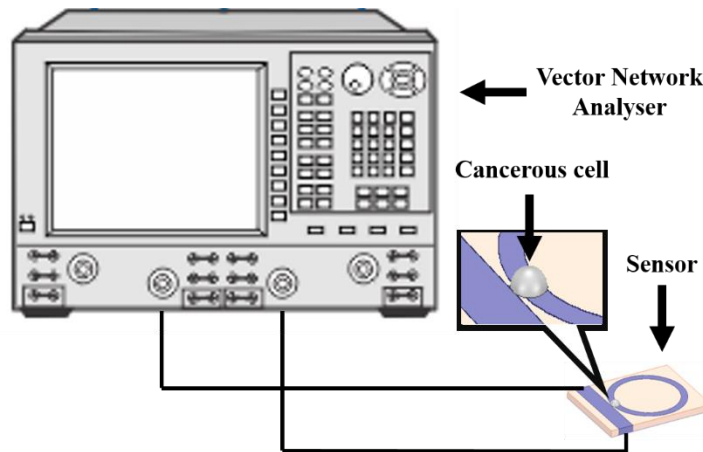


Figure 40: Schematic of the measurement setup

### 4.1 Sensor Fabrication

The laminate that was used to fabricate the sensor is FR408 from Isola [47], which has a dielectric constant of 3.687 and a thickness of 1.6 mm. The fabrication starts by exporting the HFSS into Gerber file. Then, the file is imported into the MITS Design Pro, the software provided by the same company, MITS, as the computer numerical control (CNC) machine. After adjusting the settings on the software, the CNC machine starts. MITS Auto Lab was used (Figure 41). Finally, the board is drilled, and the Sub Miniature version A (SMA) connectors are soldered to the sensor ports. The final printed design is illustrated in Figure 42.

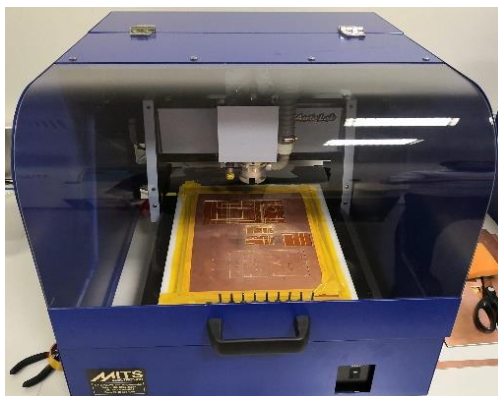
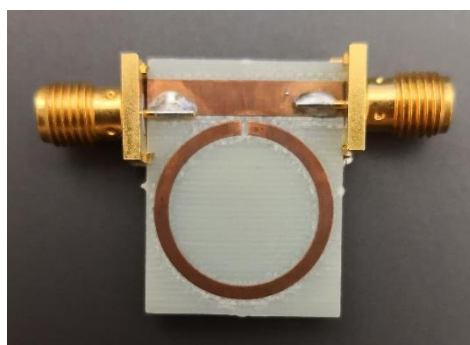
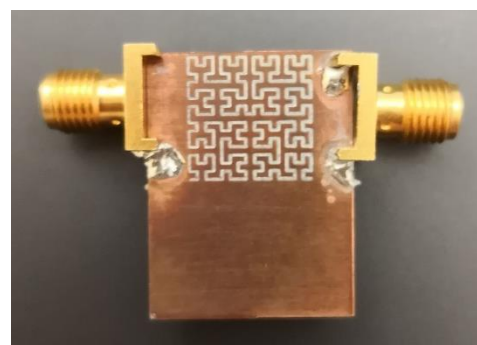


Figure 41: MIT S Auto Lab



(a) Top view



(b) Bottom view

Figure 42: Top and bottom views of the sensors

## 4.2 Cell Culture and Sample Preparation

Human breast cancer cells MDA-MB-231(HTB-26) and HS578T (HTB126) were obtained from American type culture collection (ATCC). Moreover, human breast cancer cells MCF-7 (300273) were obtained from Cell Line Service GmbH. The cells are obtained from a 10 cm dish where they were cultured and maintained in Dulbecco's Modified Eagle's Medium until they reached 85% confluency. Subsequently, the cells were washed with phosphate-buffered saline (PBS). Then, they were trypsinized and collected in a 1.5 ml tube. Next, the cells were centrifuged at 2000 rpm for 5 min. The liquid was discarded, and the pellet containing the cells were mixed and ready to be used.

### 4.3 Lab Measurement Instrument and Procedure

The measurement system is composed of R&S<sup>®</sup> ZVL VNA that has a range of 9 KHz–13.6 GHz, 50  $\Omega$  coaxial cables, calibration kit, and SMA–N connectors, as depicted in Figure 43. The connectors are used to connect the SMA calibration kit to the 50  $\Omega$  coaxial cables and the coaxial cables to the VNA.

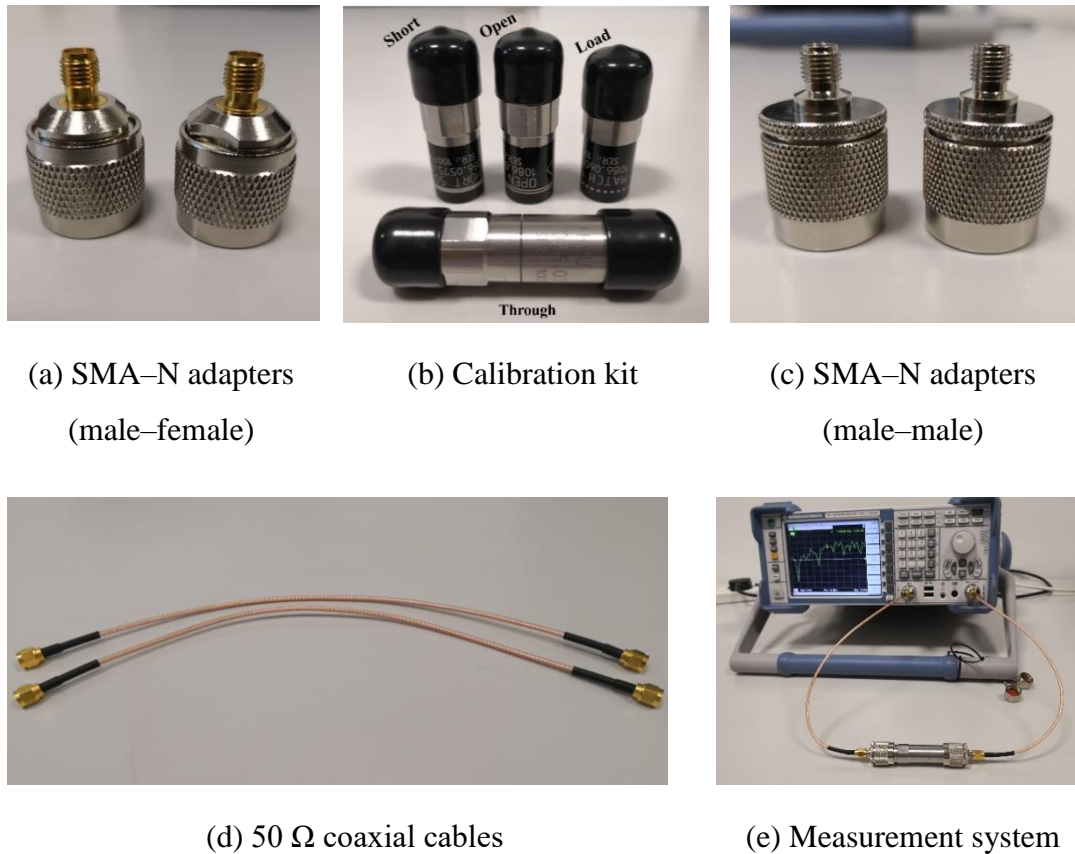


Figure 43: Lab measurement instruments

#### 4.3.1 VNA Calibration

To acquire sensor response, the sensor must be connected to a VNA. The VNA must be calibrated beforehand to remove the systematic errors, which can be added to the measurements and, therefore, produce faulty outputs. The technique applied is known as vector error correction [48]. The systematic errors are due to VNA's imperfections. Drift errors, a type of error, can occur because a change in the ambient

temperature may lead to the expansion or shrinkage of the cable size, thus producing additional errors. Furthermore, using connectors and cables adds noise, called random errors, to the system. Thus, for precise measurements, calibrating the system is an important requirement. Calibration normalizes the magnitude of and phase changes in the measurement system, thus stabilizing the reflection coefficient measured by the VNA. This process moves the measurement reference planes to the end of the measuring cables. The calibration was conducted through four calibration steps, that is, short, open, load, and thru (SOLT). The test was performed using two ports to ensure the error correction in transmission and reflection in the forward and reverse direction.

### **4.3.2 System Setup**

After the VNA calibration, the two terminals of the sensor were connected to the two ports of the VNA (Figure 44). The sensor is positioned such that it is surrounded by air because the response of the sensor will be affected by any material that comes in contact with it and will be in the same environment as the simulation. A micropipette was used to place the cells on top of the gap. Two drops were added to the sensor, thereby producing a hemispherical drop with a diameter of 2 mm. After measuring each sample, the sensor was cleaned using ethanol and was left to dry using an air pump. The measurement was performed using the vacuum and the three cancer cells, namely, MDA-MB-231, MCF-7, and HS578-T. In each case, the S-parameters ( $S_{21}$ ) were obtained, and decibels, magnitude, and phase were recorded.

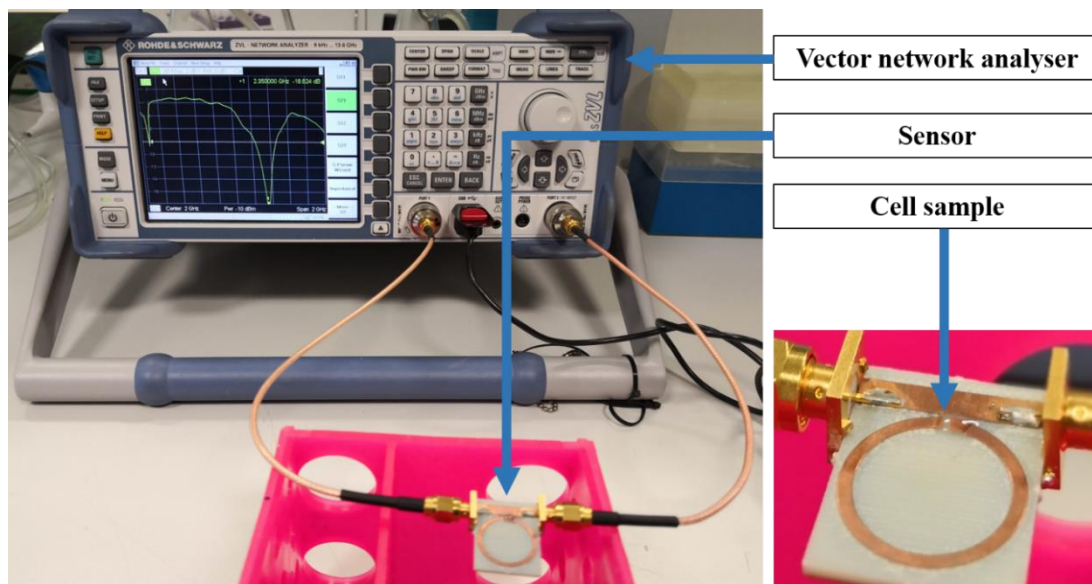
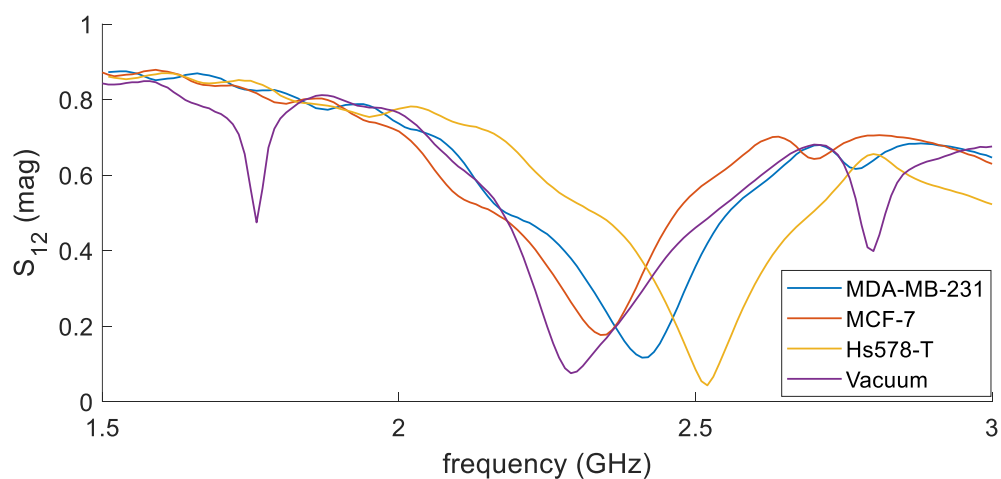


Figure 44: Measurement setup

### 4.3.3 Measurement Results

The measurement results of the transmission coefficient of MDA-MB-231, MCF-7, and HS578-T compared with the transmission coefficient of vacuum are demonstrated in Figure 45 and Figure 46. The results are presented in magnitude and phase angles with respect to frequency.

Figure 45: Measured  $S_{12}$  in magnitude



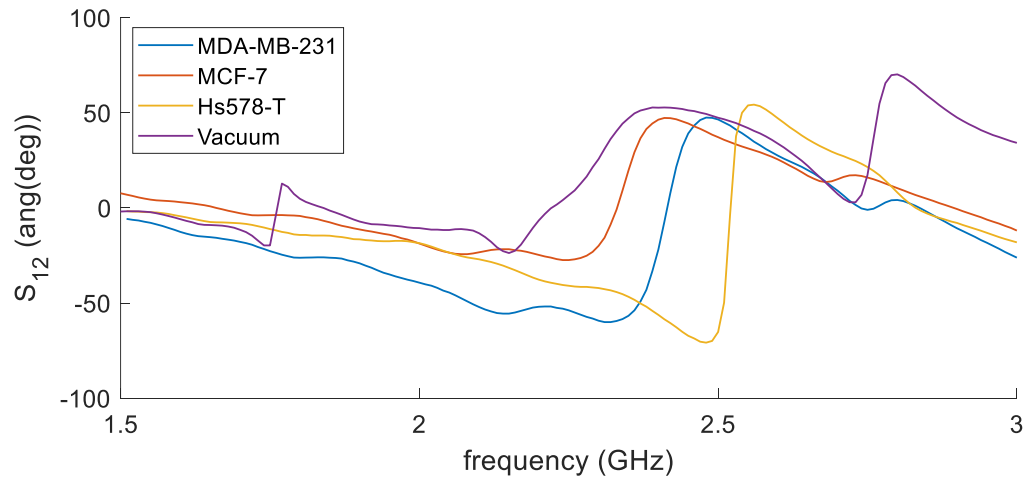


Figure 46: Measured  $S_{12}$  in phase angles

The lab measurements are compared with the simulation results. The vacuum is set as the reference, and the shift in frequency for the three cancer cell lines is calculated. Figure 47, Figure 48, Figure 49, and Figure 50 plot the comparison of the simulation and the lab measurements. The shift in frequency between the simulated and measured responses for vacuum is 0.009 GHz, as displayed in Figure 47. Moreover, the difference in the phase is  $113.73^\circ$ . Similarly, Figure 48 presents a shift of 0.01 GHz between the simulated and the measured responses for MDA-MB-231. The difference in phase angle between the simulated reflection and measured coefficients is  $73.371^\circ$ .

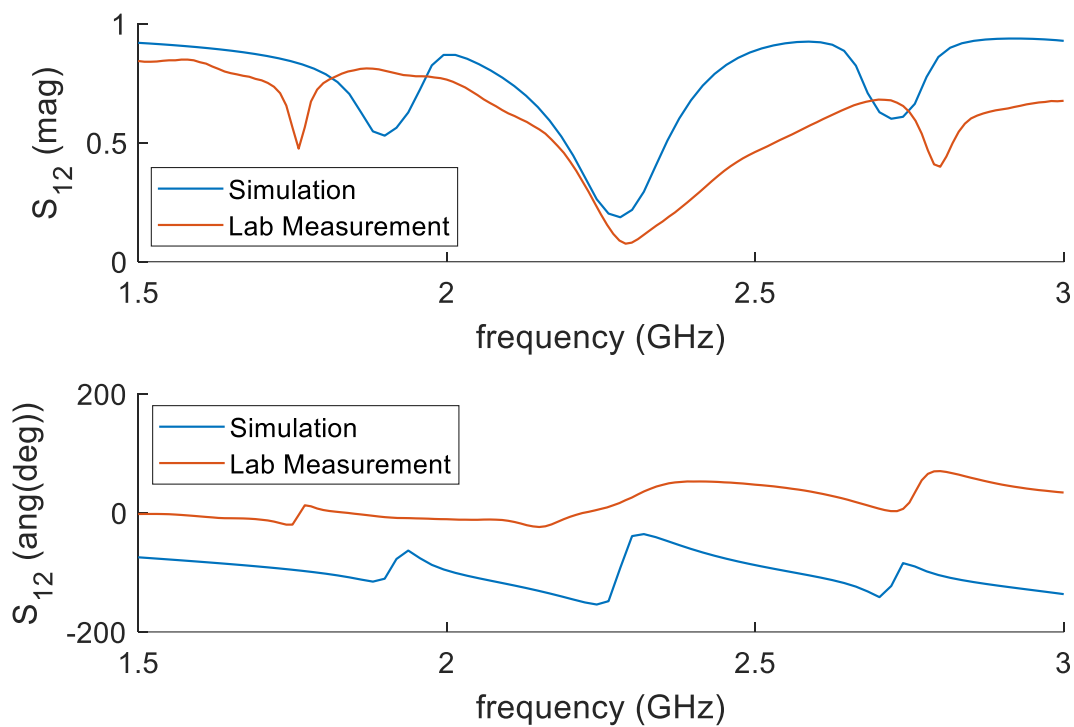


Figure 47: Transmission coefficient of vacuum

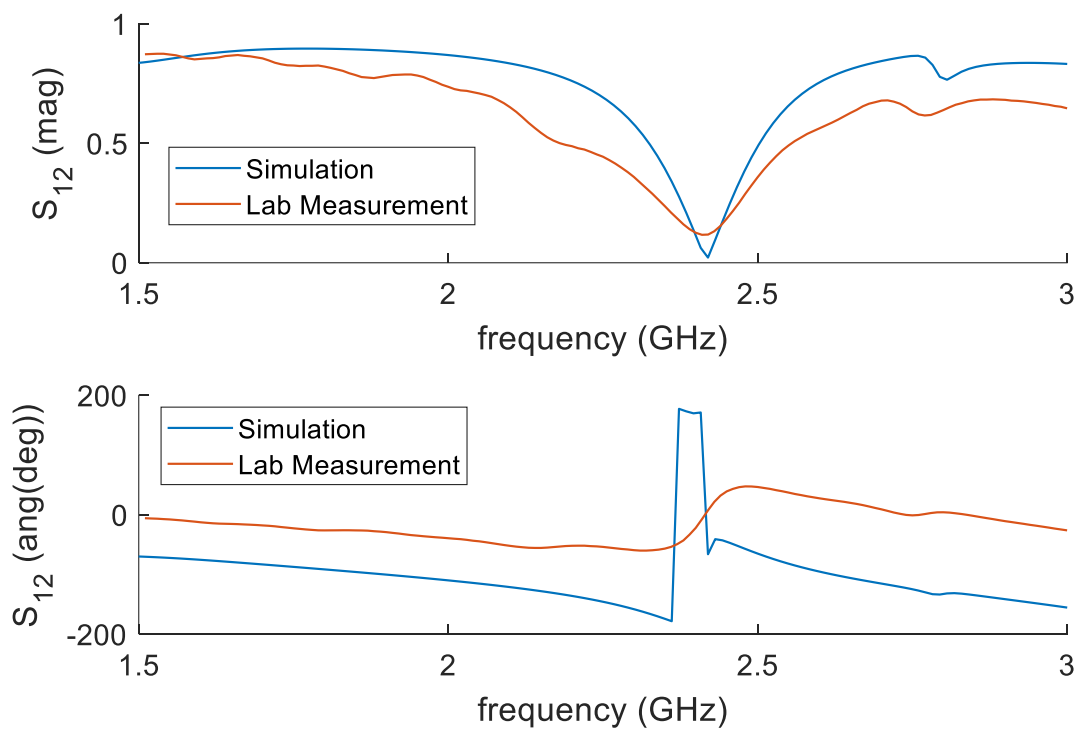


Figure 48: Transmission coefficient of MDA-MB-231

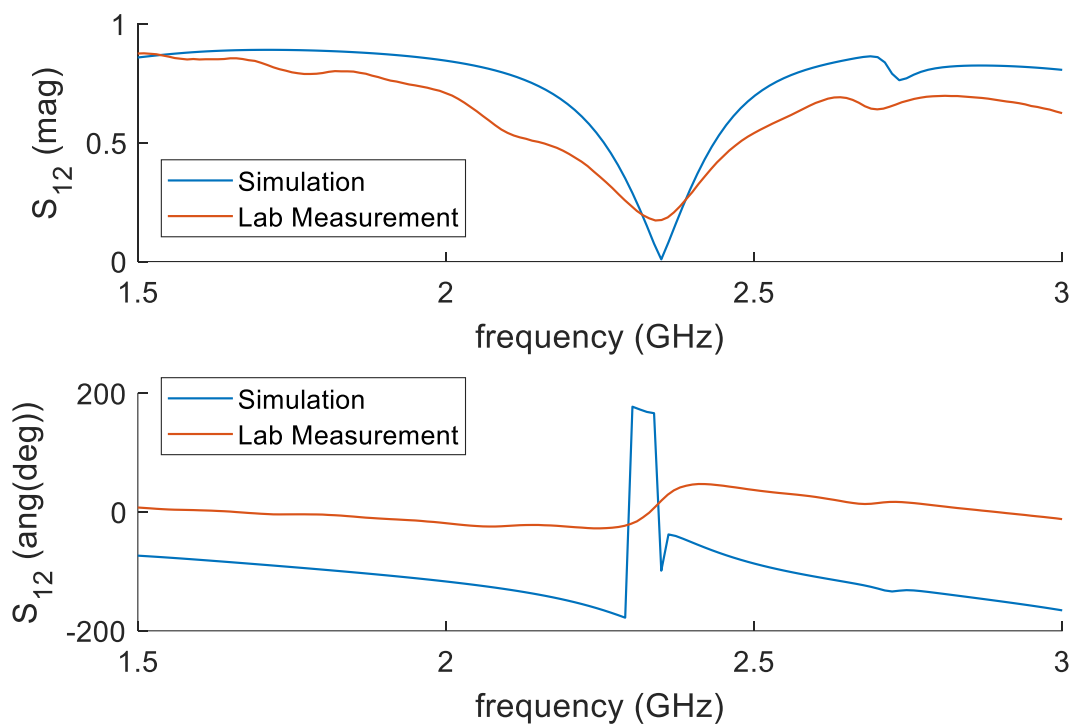


Figure 49: Transmission coefficient of MCF-7

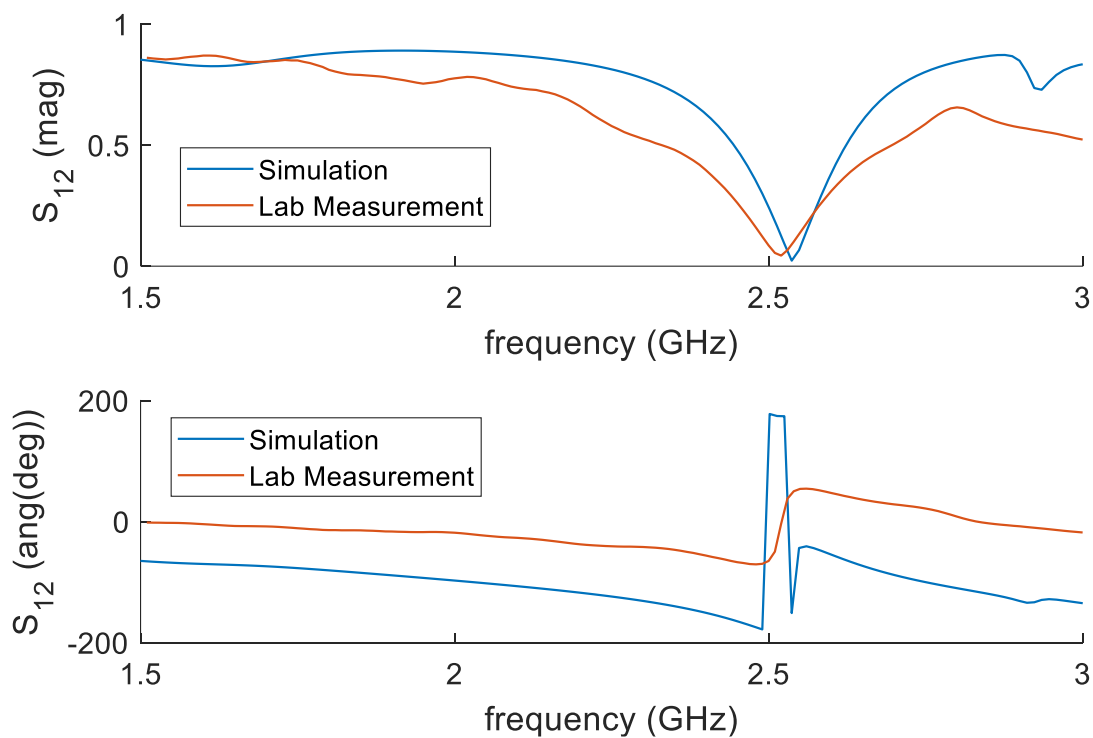


Figure 50: Transmission coefficient of HS578-T

The comparison between the measured and simulated transmission coefficients of MCF-7 is plotted in Figure 49. The difference between the simulated resonance and measured frequencies is 0.001 GHz. Moreover, the difference in magnitude is 0.1658

and  $118.4^\circ$  in terms of phase angle. Similarly, Figure 50 illustrates the simulated and measured reflection coefficients of HS578-T. The difference between the resonance frequencies is 0.017 GHz. The difference in magnitude between the obtained results is 0.0208 and  $147.64^\circ$  in terms of phase angle. The difference between the measured and simulated values can be caused by a fabrication error and calibration. SMA–N adapters were required to connect the SLOT loads to the VNA during the calibration process. After the calibration, the adapters were removed.

The parameter that had the least amount of change is the resonance frequency; the maximum shift that was obtained is 17 MHz. The difference between the measured and simulated values of the reflection coefficient is apparent. Thus, the classification method can be based on calculating the amount of shift in the resonance frequency. Table 5 summarizes the measured values and highlights the resonance frequency shift of the three cancer cell lines with respect to the vacuum resonance frequency.

Table 5: Lab measurement

	<b>MDA-MB-231</b>	<b>MCF-7</b>	<b>HS578-T</b>
<b>Frequency (GHz)</b>	2.41	2.35	2.52
<b>Magnitude</b>	0.1170	0.1750	0.0436
<b>Degree</b>	-7.37	19.7	-3.66
<b><math>\Delta f</math></b>	0.120	0.060	0.230

Table 6 lists the data that indicates a minimum difference of 60 MHz, which corresponds to the difference between MDA-MB-231 and MCF-7. The maximum shift in resonance frequency after which the cell types may be misclassified is 30 MHz.

Table 6: Variation in the resonance frequency of the lab measured values with respect to different references

		<b>HS578-T</b>	<b>MDA-MB-231</b>	<b>MCF-7</b>	<b>Vacuum</b>
	<b>Frequency (GHz)</b>	<b>2.52</b>	<b>2.41</b>	<b>2.35</b>	<b>2.29</b>
<b>Vacuum</b>	<b>2.29</b>	0.23	0.12	0.06	0
<b>MCF-7</b>	<b>2.35</b>	0.17	0.06	0	0.06
<b>MDA-MB-231</b>	<b>2.41</b>	0.11	0	0.06	0.12
<b>HS578-T</b>	<b>2.52</b>	0	0.11	0.17	0.23

#### 4.4 Cell Type Classification

In this section, we will develop an artificial neural network (ANN) to identify the type of cancer cell line based on their resonance frequency. The neural network is trained to classify the cell type based on its resonance frequency. Using the HFSS, the cancerous cell lines were simulated multiple times under different conditions. The obtained results are used to build an SVM for classification, as mentioned in Section 1.3.8, which is modeled and trained using the Classification Learner tool, which was provided by MATLAB. The training set of the model consists of three cancerous cell lines and the vacuum response with their corresponding resonance frequencies. The results of the lab measurement are used to test the model, which is a linear SVM model, which adopts the one-versus-one method. Therefore,  $\frac{K(K-1)}{2}$  binary classifiers, where  $K$  is the number of classes are used, as depicted in Figure 51.

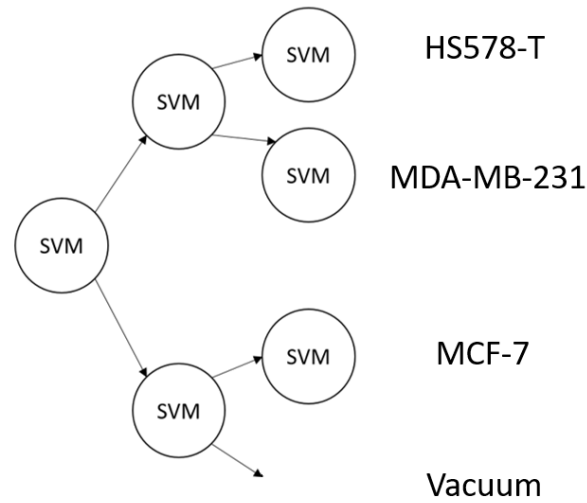


Figure 51: One-versus-one multiclassification method

Table 7: Resonance frequencies used as a training set (GHz)

HS578-T		MDA-MB-231	
2.5010	2.5337	2.4054	2.4134
2.5040	2.5338	2.4055	2.4271
2.5162	2.5347	2.4064	2.4304
2.5186	2.5379	2.4087	2.4391
2.5278	2.5163	2.4090	2.4073
MCF-7		Vacuum	
2.3320	2.3573	2.2935	2.2910
2.3424	2.3595	2.2901	2.2922
2.3460	2.3598	2.2856	2.2884
2.3466	2.3604	2.2849	2.2863
2.3533	2.3603	2.2942	2.2875

The training data, which are presented in Table 7, are inputted into MATLAB. Subsequently, the Classification Learner tool is launched, and the training table is loaded into the tool. One column is selected as the predictor that contains the resonance frequencies. The other column is selected as the response that contains the corresponding class number, which represents the cancerous cell line types, as demonstrated in Figure 52. Class 1 corresponds to HS578-T, Class 2 to MDA-MB-231, Class 3 to MCF-7, and Class 4 to vacuum.

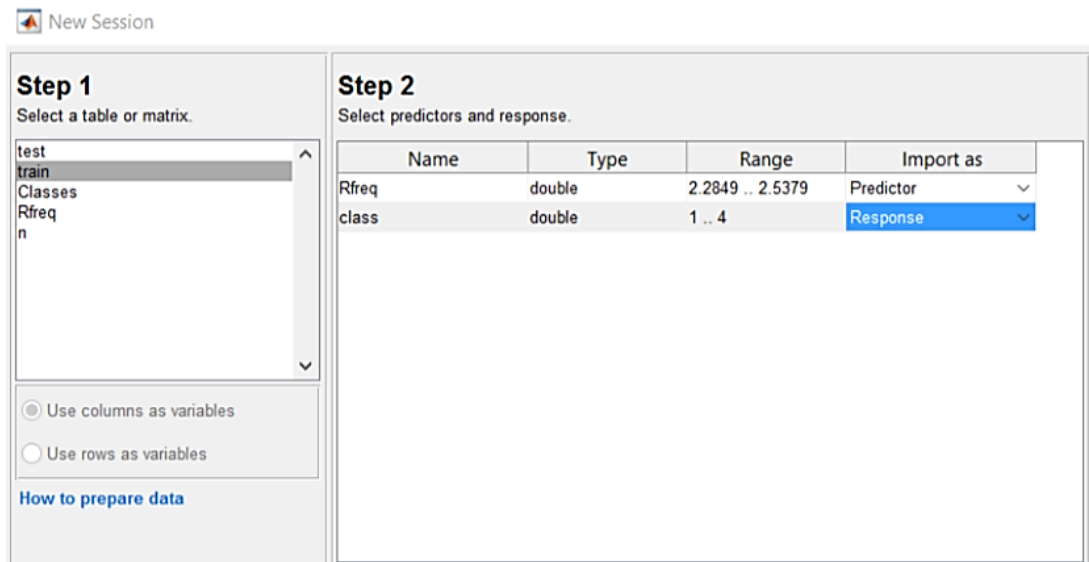


Figure 52: Classification Learner

After starting the session, the set is trained using all SVM models: linear, quadratic, cubic, fine Gaussian, medium Gaussian, and coarse Gaussian. All models showed 100% accuracy, as exhibited in Figure 53. The linear classifier is exported to MATLAB's workspace because the classifier is the simplest model. The time required to train in the classifier is 4.7892 s, and the prediction speed is approximately 95 obs/s.

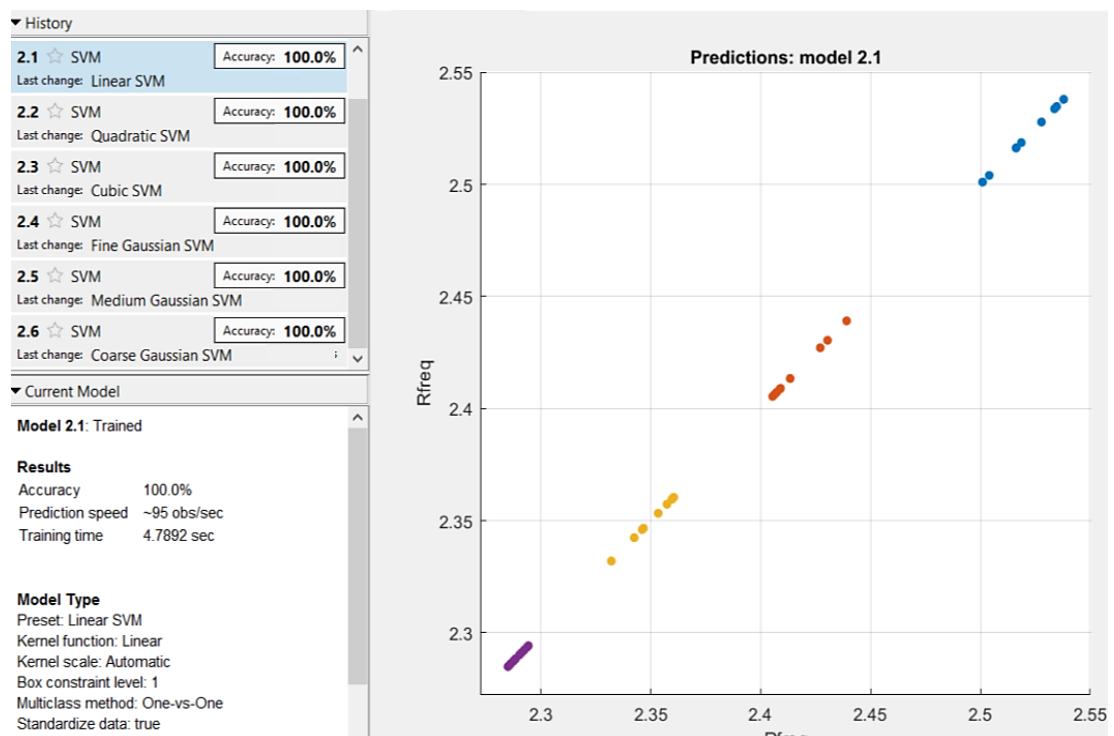


Figure 53: Linear SVM scatterplot

Consequently, the resonance frequencies obtained from the lab measurement are delivered to the classifier. Accordingly, the frequencies are classified into their perspective type, as displayed in Figure 54.

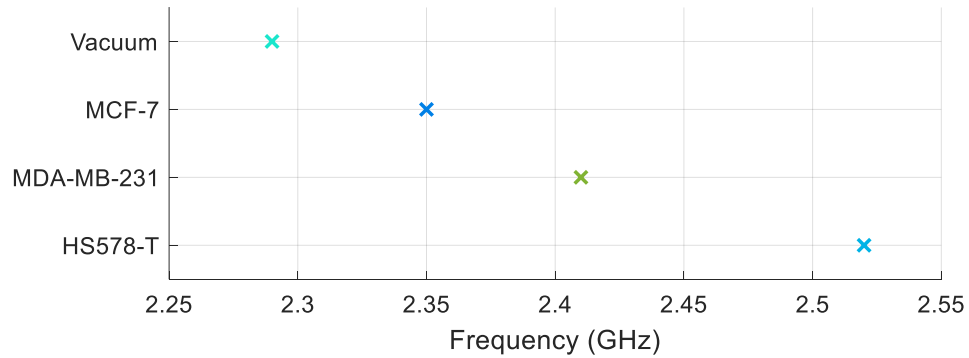


Figure 54: Classified resonance frequencies

#### 4.5 Confidence Interval

In this section, the confidence interval (CI) is calculated for the three cancerous cell lines along with the vacuum. The samples were measured under different conditions. The obtained results are averaged, and their 95% confidence level is calculated as presented in Figure 55, Figure 56, Figure 57, and Figure 58. Eq. (15) defines the equation that was used to generate the confidence level, where  $\bar{x}$  is the averaged signal,  $z$  is the optimal confidence level,  $\sigma$  is the standard deviation, and  $n$  is the sample size.

$$CI = \bar{x} \pm z \frac{\sigma}{\sqrt{n}} \quad (15)$$

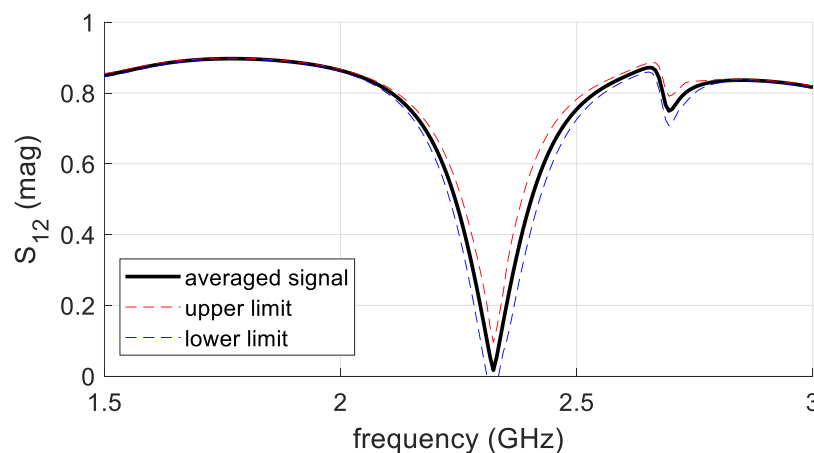


Figure 55: Averaged response of MCF-7 and its confidence interval



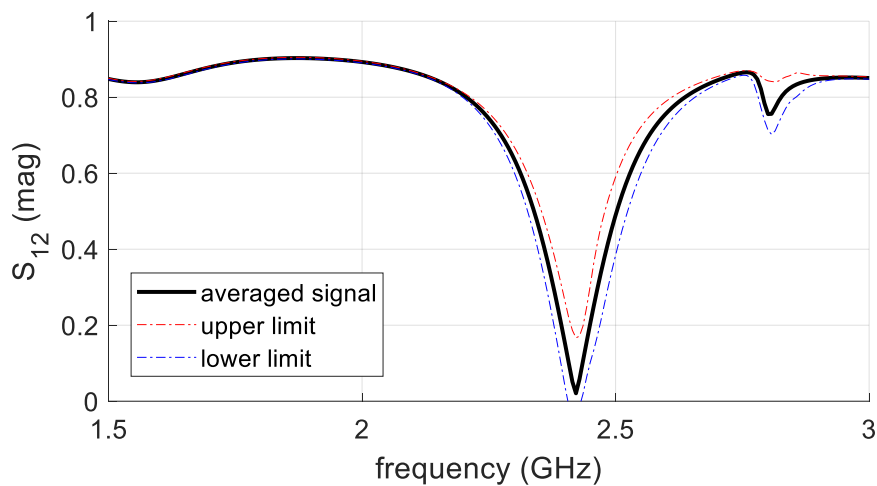


Figure 56: Averaged response of MDA-MB-231 and confidence interval

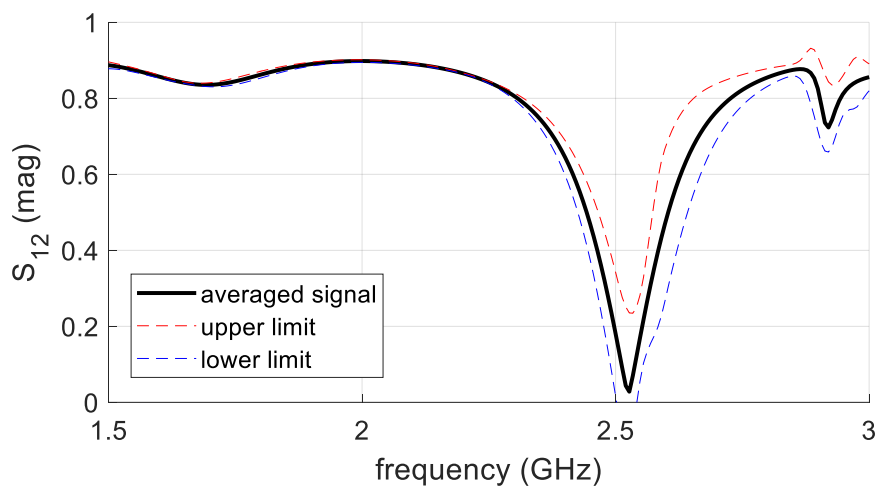


Figure 57: Averaged response of HS578-T and its confidence interval

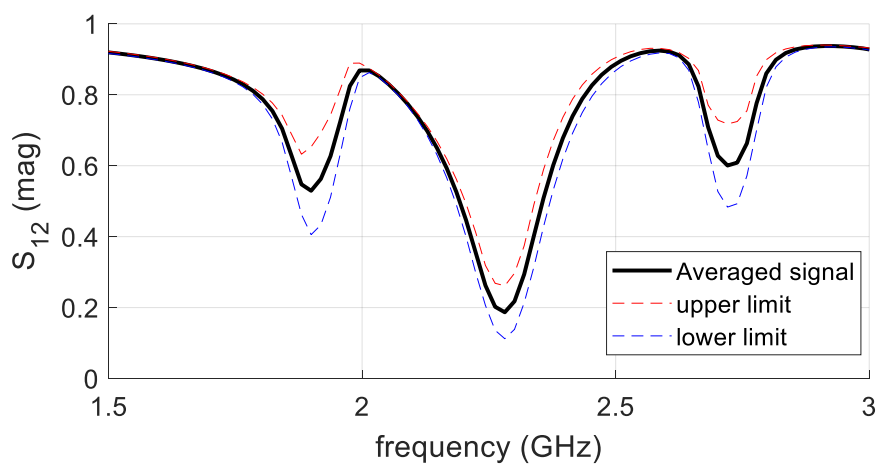


Figure 58: Averaged response of vacuum and its confidence interval

## Chapter 5: Conclusion and Future Work

In summary, a biosensor was designed to detect different types of cancerous cell lines based on their electrical properties. The microstrip-based sensor that was proposed consists of a single circular SRR with a Hilbert fractal curve as a DGS. The SRR is known for its behavior that is similar to the LC circuits, which are known for their ability to generate or acquire a signal with a specific frequency. Moreover, SRRs are known for their flexibility. Furthermore, the SRR gap produced a high capacitance when a current passes through the ring. This high capacitance reduced the resonance frequency but increased the resonance wavelength. Therefore, the SRR structure was smaller in size than the targeted wavelength. Moreover, the high capacitance induced at the gap allowed the SRR to be used as a sensor because changing the medium of the gap would modify the capacitance, thereby causing a shift in the resonance frequency. The frequency shift was used to indicate the type of material. The DGS was used to redistribute the current in the sensor, such that the capacitance increased at the gap, thus reducing the resonance frequency. When the SRR was designed to be small, its corresponding frequency was in a higher range than the targeted range. The addition of the DGS lowered the resonance frequency. The DGS that was used was a Hilbert fractal curve given its folding property, which allows the DGS to be smaller than  $1/10$  of the targeted wavelength. In the early stage of designing, different Hilbert orders were tested. First, second, third, and fourth orders were tested as the DGS. The fourth order has the strongest electrical and magnetic field, thereby leading to high sensitivity. In the first stage, the sensor was designed theoretically using the mathematical model. The resonance frequency, capacitance, and inductance were obtained for the SRR. Then, the same parameters were obtained for the perturbed fourth-order Hilbert fractal ground. Subsequently, the parallel combinations of the capacitance and inductance were obtained to acquire the resonance frequency of the combined design using the

LC circuit model. In the next stage, all SRRs, the perturbed fourth-order Hilbert ground, and the combined design were simulated using the HFSS to confirm the acquired results from the theoretical model. The mathematical and simulated models of the SRR had the same resonance frequency. However, for the perturbed Hilbert ground, a percentage difference of 2.09% is noticeable. Similarly, the combined design had a percentage difference of 1.24% between the simulated and calculated resonance frequencies. Prior to the fabrication, the operation of the sensor was simulated using three types of cancerous cell lines, namely, HS578-T, MCF-7, and MDA-MB-231, along with the vacuum. The operation was performed by inputting the electrical properties of the cells into the software. We obtained clear results by examining the transmission coefficient; thus, all the results were viewed using the transmission coefficient. Consequently, the microstrip-based sensor was fabricated using the MITS Auto Lab. Then, the sensor was tested using the three types of cancerous cell lines. The results obtained from the lab measurements were used to test the SVM, which was developed to classify the cells based on their resonance frequency. The SVM was trained using data obtained from simulating the sensor under different conditions. The SVM was able to classify the measured resonance frequencies correctly into their corresponding cancerous cell line. In the future, the design can be integrated into other components, such as a transmitter and a receiver, to create a standalone device.

## References

- [1] American Cancer Society, "Cancer Facts & Figures," American Cancer Society Inc., Atlanta, 2018.
- [2] "Ultrasound," Medline Plus, 17 July 2018. [Online]. Available: <https://medlineplus.gov/ultrasound.html>. [Accessed 4 October 2018].
- [3] "Magnetic Resonance Imaging (MRI) - Breast," [Online]. Available: <https://www.radiologyinfo.org/en/info.cfm?pg=breastmr>. [Accessed 15 February 2018].
- [4] D. Jithin et al., "Dielectric characterization of breast cancer cell lines using microwaves," in *5th International Conference on Electronic Devices, Systems and Applications (ICEDSA)*, Ras Al Khaimah, 2016.  
DOI: 10.1109/ICEDSA.2016.7818559
- [5] M. Cavagnaro et al., "A model to evaluate dielectric properties of human tissues based on water content," in *8th International Symposium on Medical Information and Communication Technology (ISMICT)*, Firenze, 2014.  
DOI: 10.1109/ISMICT.2014.6825221
- [6] A. Surowiec et al., "Dielectric properties of breast carcinoma and the surrounding tissues," *IEEE Transactions on Biomedical Engineering*, vol. 35, no. 4, pp. 257-263, 1988. DOI: 10.1109/10.1374
- [7] A. Albishi and O. M. Ramahi, "Microwaves-based high sensitivity sensors for crack detection in metallic materials," *IEEE Transactions on Microwave Theory and Techniques*, vol. 65, no. 5, pp. 1864-1871, 2017.  
DOI: 10.1109/TMTT.2017.2673823
- [8] M. Hussein et al., "Microwave Characterization of Hydrophilic and Hydrophobic Plant Pathogenic Fungi Using Open-Ended Coaxial Probe," *IEEE Access*, vol. 7, pp. 45841 - 45849, 2019. DOI: 10.1109/access.2019.2908061
- [9] N. Maode et al., "An improved open-ended waveguide measurement technique on parameters epsilon of high-loss materials," *IEEE Transactions on Instrumentation and Measurement*, vol. 47, no. 2, p. 476, 1998.

- [10] C. Chang, J. Chen and T. Wu, "Dielectric Modeling of Asphalt Mixtures and Relationship with Density," *Journal of Transportation Engineering*, vol. 137, no. 2, pp. 104-111, 2011. DOI: 10.1061/(ASCE)TE.1943-5436.0000204
- [11] P. Quéffélec et al, "Detection of micro-cracks on metal surfaces using near-field microwave dual-behaviour resonators," in *New Developments and Applications in Sensing Technology*, Berlin, Springer Berlin Heidelberg, 2011, pp. 1-13. DOI: 10.1007/978-3-642-17943-3
- [12] R. Kshetrimayum, "A brief intro to metamaterials," *IEEE Potentials*, vol. 23, no. 5, pp. 44-46, 2004. DOI: 10.1109/MP.2005.1368916
- [13] Gay-Balmaz, Philippe, and Olivier J. F Martin, "Electromagnetic Resonances in Individual and Coupled Split-Ring Resonators," *Journal of Applied Physics*, vol. 92, no. 5, pp. 2929-2936, 2002. DOI: 10.1063/1.1497452
- [14] G. Galindo-Romera et al, "Submersible Printed Split-Ring Resonator-Based Sensor for Thin-Film Detection and Permittivity Characterization," *IEEE Sensors Journal*, vol. 16, no. 10, pp. 3587-3596, 2016. DOI: 10.1109/JSEN.2016.2538086
- [15] R. Marques et al, "Comparative Analysis of Edge- and Broadside- Coupled Split Ring Resonators for Metamaterial Design - Theory and Experiments," *IEEE Transactions on Antennas and Propagation*, vol. 51, no. 10, pp. 2572-2581, 2003. DOI: 10.1109/TAP.2003.817562
- [16] S. Gamouh and A. Chaabi, "Microwave biosensor based on a double metamaterial particle," in *4th International Conference on Control Engineering & Information Technology (CEIT)*, Hammamet, 2016. DOI: 10.1109/CEIT.2016.7929122.
- [17] J. Russer, "Printed self-complementary hilbert curve (SCHC) fractal broad-band antenna," in *2018 Baltic URSI Symposium (URSI)*, Poznan, 2018. DOI: 10.23919/URSI.2018.8406743.
- [18] "Hilbert Curves," Data Genetics, 2013. [Online]. Available: <http://datagenetics.com/blog/march22013/index.html>. [Accessed 20 September 2018].

- [19] P. Séébold, "Tag-systems for the Hilbert curve," *Discrete Mathematics and Theoretical Computer Science*, *Discrete Mathematics and Theoretical Computer Science*, vol. 9, no. 2, pp. 213 - 226, 2007.
- [20] S. Rehman et al, "Compact Bandpass Filters with Bandwidth Control Using Defected Ground Structure (DGS)," *Applied Computational Electromagnetics Society Journal*, vol. 26, no. 7, pp. 624-630, 2011.
- [21] D. Guha et al, *Microstrip and Printed Antennas New Trends, Techniques and Applications.*, John Wiley & Sons Inc, 2011.
- [22] "3D Electromagnetic Field Simulator for RF and Wireless Design," ANSYS, 2018. [Online]. Available: <https://www.ansys.com/products/electronics/ansys-hfss>. [Accessed 24 September 2018].
- [23] Tektronix, "Introduction to VNA Basics," March 2017. [Online]. Available: <https://www.tek.com/document/primer/what-vector-network-analyzer-and-how-does-it-work>. [Accessed 24 September 2018].
- [24] M. Atif et al, "Spectral characterization of breast cancer," in *11th Annual High Capacity Optical Networks and Emerging/Enabling Technologies* , Charlotte, 2014. DOI: 10.1109/HONET.2014.7029390
- [25] Y. Kimura et al, "The development of real-time PCR micro device with optical sensor for early detection of cancer," in *38th Annual International Conference of the IEEE Engineering in Medicine and Biology Society*, Orlando, 2016. DOI: 10.1109/EMBC.2016.7592030
- [26] W. Ali et al, "Differentiating Metastatic and Non-metastatic Tumor Cells from Their Translocation Profile through Solid-State Micropores," *Langmuir : The ACS Journal of Surfaces and Colloids*, vol. 32, no. 19, pp. 4924-4934, 2016. DOI: 10.1021/acs.langmuir.6b00016
- [27] I. Rusni and A. Ismail, "Aligned gap multiple split ring resonator biosensor for DNA hybridization detection at microwave frequency," in *6th International Conference on Electrical Engineering and Informatics (ICEEI)*, Langkawi, 2017.

- [28] H. Lee et al, "DNA sensing based on single element planar double split-ring resonator," in *2009 IEEE MTT-S International Microwave Symposium Digest*, Boston, 2009. DOI: 10.1109/MWSYM.2009.5166039
- [29] R. Melik et al, "Metamaterial-based wireless RF-MEMS strain sensors," in *2010 IEEE Sensors*, Kona, 2010. DOI: 10.1109/ICSENS.2010.5690582
- [30] J. Li et al, "Metamaterial-based strain sensors," in *7th International Conference on Intelligent Sensors, Sensor Networks and Information Processing (ISSNIP)*, Adelaide, 2011. DOI: 10.1109/ISSNIP.2011.6146571
- [31] L. La Spada, F. Bilotti and L. Vegni, "Metamaterial biosensor for cancer detection," in *2011 IEEE SENSORS Proceedings*, Limerick, 2011. DOI: 10.1109/ICSENS.2011.6127103
- [32] M. Asad et al, "Single port bio-sensor design using metamaterial split ring resonator," in *2016 5th International Conference on Electronic Devices, Systems and Applications (ICEDSA)*, Ras Al Khaimah, 2016. DOI: 10.1109/ICEDSA.2016.7818515
- [33] S. Hardinata et al, "Biosensor miniaturization for non-invasive measurements of materials and biological tissues," in *2017 International Seminar on Sensors, Instrumentation, Measurement and Metrology (ISSIMM)*, Surabaya, 2017. DOI: 10.1109/ISSIMM.2017.8124278
- [34] A. Alghamdi and S. Mohammadi, "A Highly Sensitive RF Biosensor Based on Splitter/Combiner Configuration for Single-Cell Characterization," in *2018 IEEE International Microwave Biomedical Conference (IMBioC)*, Philadelphia, PA, 2018. DOI: 10.1109/IMBIOC.2018.8428863
- [35] N. Sharafadinzadeh, M. Abdolrazzagli and M. Daneshmand, "Highly sensitive microwave split ring resonator sensor using gap extension for glucose sensing," in *IEEE MTT-S International Microwave Workshop Series on Advanced Materials and Processes for RF and THz Applications (IMWS-AMP)*, Pavia, 2017. DOI: 10.1109/IMWS-AMP.2017.8247400

- [36] S. Harnsoongnoen, U. Charoen-In and A. Wanthong, "Determination of glucose concentration with resonant coplanar microwave sensor," in *2017 International Electrical Engineering Congress (iEECON)*, Pattaya, 2017.  
DOI: 10.1109/IEECON.2017.8075895
- [37] T. Yun and S. Lim, "High-Q and miniaturized complementary split ring resonator-loaded substrate integrated waveguide microwave sensor for crack detection in metallic materials," *Sensors & Actuators: A. Physical*, vol. 214, pp. 25-30, 2014. DOI: 10.1016/j.sna.2014.04.006
- [38] D. Kim, C. Kim and D. Yang, "Flexible Hilbert-Curve Loop Antenna Having a Triple-Band and Omnidirectional Pattern for WLAN/WiMAX Applications," *International Journal of Antennas and Propagation*, vol. 2012, no. 16875869, pp. 1-9, 2012. DOI: 10.1155/2012/687256
- [39] A. Karmakar et al, "An UWB antenna using modified Hilbert curve slot for dual band notch characteristics," *Journal of Electromagnetic Waves and Applications*, vol. 27, no. 13, pp. 1620-1631, 2013. DOI: 10.1080/09205071.2013.821676
- [40] V. Radonić, G. Kitić and V. Crnojević-Bengin, "Novel hilbert soil-moisture sensor based on the phase shift method," in *10th Mediterranean Microwave Symposium*, Guzelyurt, 2010. DOI: 10.1109/MMW.2010.5605150
- [41] U. Khayam and F. Alfaruq, "Design of hilbert antenna as partial discharge sensor," in *2nd International Conference of Industrial, Mechanical, Electrical, and Chemical Engineering*, Yogyakarta, 2016.  
DOI: 10.1109/ICIMECE.2016.7910419
- [42] M. A. Darmawan and U. Khayam, "Design, simulation, and fabrication of second, third, and forth order hilbert antennas as ultra high frequency partial discharge sensor," in *Proceedings of the Joint International Conference on Electric Vehicular Technology and Industrial, Mechanical, Electrical and Chemical Engineering*, Surakarta, 2015.  
DOI: 10.1109/ICEVTIMECE.2015.7496707
- [43] M. Harbaji et al, "Design of Hilbert Fractal Antenna for Partial Discharge Classification in Oil-Paper Insulated System," *IEEE Sensors Journal*, vol. 17, no. 4, pp. 1037-1045, 2017. DOI: 10.1109/JSEN.2016.2638804



- [44] B. Sauviac, C. Simovski and S. Tretyakov, "Double Split-Ring Resonators: Analytical Modeling and Numerical Simulations," *Electromagnetics*, vol. 24, no. 5, pp. 317-338, 2004. DOI: 10.1080/02726340490457890
- [45] M. Sadiku, S. Musa and S. Nelatury, "Comparison of approximate formulas for the capacitance of microstrip line," in *Proceedings 2007 IEEE SoutheastCon*, Richmond, 2007. DOI: 10.1109/SECON.2007.342939
- [46] K. Wang et al, "Resonant frequency and sensitivity analysis of hilbert curve fractal antennas for DRM communications," in *8th International Symposium on Antennas, Propagation and EM Theory*, Kunming, 2008.  
DOI: 10.1109/ISAPE.2008.4735159
- [47] "FR408: High Performance Laminate and Prepreg," Isola, [Online]. Available: <https://www.isola-group.com/products/all-printed-circuit-materials/fr408/>. [Accessed 19 January 2019].
- [48] M. Hiebel, "Vector network analyzer (VNA) calibration: the basics," Rohde and Schwarz, 2008.